Planetary and Space Science 283 (2026) 106344

Contents lists available at ScienceDirect

Planetary and Space Science

journal homepage: www.elsevier.com/locate/pss

Study of the spatial sensitivity of the VenSpec-U spectral imager onboard EnVision using an instrumental model

Lucile Conan [a], Emmanuel Marcq [a,*], Benjamin Lustrement [a], Maxence Lefèvre [a], Nicolas Rouanet [a], Baptiste Leduc [a], Abraham Diaz Damian [a], Lucio Baggio [a], Sandrine Bertran [b], Séverine Robert [c], Océane Barraud [d], Giulia Alemanno [d]

[a] LATMOS/IPSL, UVSQ Université Paris-Saclay, Sorbonne Université, CNRS, Guyancourt, France
[b] Hensoldt Space Consulting, Guyancourt, France
[c] Royal Belgian Institute for Space Aeronomy (BIRA-IASB), Brussels, Belgium
[d] DLR Institute of Planetary Research, Berlin, Germany

ARTICLE INFO

Keywords:
Instrumentation
Modeling
Venus

ABSTRACT

The VenSpec-U spectrometer onboard EnVision will be dedicated to the study of Venus' upper atmosphere, with four main science goals: monitoring the sulfured species SO_2 and SO, the UV absorber, and performing observations of the cloud-top with a high spatial resolution thanks to a pushbroom observation strategy. In this article, we study the imaging capabilities of the instrument, as part of the global performance assessments undertaken to estimate the compliance of the current design with the science requirements. This work involves a combination of models to simulate the whole acquisition process, from the observed scene at the cloud-top of Venus, to the consideration of the instrument's behavior inducing degradation of the images and spectra: outputs of a Large Eddy Simulation model are used to compute maps of atmospheric parameters related to VenSpec-U's science goals; a radiative transfer model (RTM), initially developed for the SPICAV/Venus Express data analysis and adapted for VenSpec-U, translates these parameters into spectral radiance maps; and a newly developed instrument forward model simulates the optics and detector effects as well as onboard data processing steps. By modifying the maps of RTM parameters, we assess contrast limits below which the small-scale variations of the atmospheric properties can no longer be retrieved accurately. We then evaluate these thresholds under various conditions, including different latitudes, spacecraft altitudes, and spatial samplings. These detection limits appear in accordance with the expected performance.

1. Introduction

Various dynamical processes are observable in the UV range at the cloud-top of Venus, including large planetary-scale contrasts as well as small-scale features. Such small-scale observations as well as the monitoring of the atmospheric variability on a planetary scale have previously been performed by the VMC/Venus Express (Markiewicz et al., 2007) and UVI/Akatsuki (Yamazaki et al., 2018) imagers. At low latitudes, mottled patterns with spatial extents down to a few tens of km have been observed, resulting from the convection caused by solar heating. Toward higher latitudes, the patterns become streakier, following the laminar flows of these regions (Titov et al., 2012). These patterns were identified as gravity waves, with wavelengths ranging from 3 to 21 km (Piccialli et al., 2014). The presence of some of these waves near high surface elevations indicates a possible orographic origin. However, convective instabilities in the lower atmosphere as well as Kelvin–Helmholtz instabilities are also potential causes of waves (Peralta et al., 2008; Tellmann et al., 2012; Lefèvre et al., 2017). As these small-scale processes can influence the energy transport mechanisms and distribution of chemical species, studying them across a wide wavelength range would help identify whether the observed patterns reflect vertical variations of the cloud-top causing shadows, or variations in the spatial distribution of the species present in the cloud layer. This would allow a more comprehensive understanding of the interactions between Venus' atmospheric dynamics and chemistry.

The investigation of the coupling processes between the atmospheric dynamics and chemistry, enabled by these high spatial resolution observations, are encompassed in the "Climate" science theme of the future EnVision mission (Widemann et al., 2023). Through this topic, the mission aims to explain the high variability of the atmosphere

* Corresponding author.
E-mail address: emmanuel.marcq@latmos.ipsl.fr (E. Marcq).

https://doi.org/10.1016/j.pss.2026.106344
Received 21 May 2026; Received in revised form 27 August 2026; Accepted 1 September 2026
Available online 16 September 2026
0032-0633/© 2026 The Authors. Published by Elsevier Ltd. This is an open access article under the CC BY license (http://creativecommons.org/licenses/by/4.0/).

and to explore its possible causes, whether they arise from external forcing like volcanism or are internal to the atmosphere. Among EnVision's payload, that will provide a global overview of the planet, the UV channel of the VenSpec suite (Helbert et al., 2019), VenSpec-U, will be dedicated to the cloud-top atmosphere and study its composition and dynamical properties. Its science goals will include in particular the observation of small-scale features at the cloud-top.

In the context of the instrument's ongoing development, that involves general performance assessments to estimate the compliance between the currently planned design and the science requirements, the imaging capabilities of the instrument should be studied. This article presents the methodology implemented for this purpose: a combination of several models is used to simulate the process of images formation and data acquisition by VenSpec-U, coupled to an inversion algorithm that allows ultimately the estimation of the quality of the retrieval of the targeted atmospheric properties. After summarizing the instrument's concept and science goals in Section 2, Section 3 presents the method used to simulate the scenes that could be observed, which consist in spectral maps of Venus' cloud-top. Section 4 then describes the instrument model that simulates the various instrumental effects impacting the acquisitions, and Section 5 presents the inversion process allowing the retrieval of VenSpec-U's key scientific products. Finally, the performance of the instrument in terms of detection of small-scale atmospheric features is evaluated in Section 6.

2. The VenSpec-U spectral imager

The UV spectral imager VenSpec-U has already been extensively described in previous Refs. Lustrement et al. (2024), Conan et al. (2024) and Marcq et al. (2021). For the reader's convenience, its main goals and characteristics are briefly summarized hereafter.

2.1. Scientific objectives

VenSpec-U aims to characterize the spatial and temporal variability of sulfured gases, regarding in particular sulfur dioxide (SO_2) and the product of its photochemical dissociation, sulfur monoxide (SO), by monitoring their column densities above the clouds. The sulfur chemistry can be investigated through the simultaneous and collocated assessment of SO_2 column above the cloud-top and the SO/SO_2 columnar abundance ratio. We also aim to monitor the "unknown UV absorber", in order to study its chemical nature and relationship with the sulfur cycle. Lastly, taking advantage of the low polar orbit of EnVision (with an inclination between 87 and 89°, and altitudes ranging from 220 to 510 km, resulting in an orbital period of 94 min), observations at high spatial resolution will be performed in order to observe the small-scale dynamical features at cloud-top level, in particular gravity waves and convection cells, so that coupling between atmospheric chemistry and dynamics can be better modeled and understood.

2.2. Operations and instrumental design

To perform such measurements, the instrument will operate on the dayside of Venus using a pushbroom strategy in a nadir or near-nadir geometry, and will observe the UV solar light backscattered by the clouds. Radiance factor of Venus' atmosphere $\beta(\lambda)$ will then be estimated using the measured radiance $I(\lambda)$ and the knowledge of the incoming solar spectral irradiance $F_\odot(\lambda)$: $\beta(\lambda) = \frac{I(\lambda) \times \pi \text{ sr}}{F_\odot(\lambda)}$. The knowledge of the solar irradiance is therefore necessary to derive Venus' radiance factor and should be provided by external estimations, either measured by a dedicated instrument, or modeled. A reference spectra derived from SOLAR-SOLSPEC data (Meftah et al., 2018) is here considered.

The instrument is composed of two channels, with a similar design (Fig. 1) but dedicated to different science goals. The *LR* (Low Resolution) channel will operate in the 190–380 nm wavelength range with a spectral resolution of 2–5 nm. It will cover the common absorption bands of SO and SO_2 centered on 220 nm as well as the broad absorption band of the UV absorber expected around 365 nm, and will allow observations of the cloud-top at a high spatial resolution, namely with samplings from 3 to 5 km. The *HR* (High Resolution) channel will operate on a narrower wavelength range, between 205 and 235 nm with a targeted spectral resolution of 0.3 nm, which will allow the distinction of SO and SO_2 absorption lines and thus the separate determination of the abundance of these two species. The spatial sampling will however be coarser, ranging from 12 to 24 km, primarily for keeping a high enough signal-to-noise ratio. Each channel will consist of an entrance baffle to limit external straylight, a two-lenses objective including a stop diaphragm, a slit delimiting the instantaneous 20° wide transverse field of view, followed by a wavelength short-pass filter and a spherical holographic grating. Images of both channel will be formed onto a common CMOS backside-illuminated detector whose temperature will be controlled by a Peltier cooler.

3. Simulations of the Venusian cloud-top atmosphere at a high spatial resolution

In order to generate the images that would be provided by VenSpec-U, scenes observable by the instrument at Venus' cloud-top must first be modeled.

3.1. Turbulent modeling of the cloud-top

The Large-Eddy Simulation (LES) mode from the Venus WRF Planetary Climate Model described by Lefèvre et al. (2024) is used to provide mesoscale simulations of the abundance of the main chemical species present in the cloud convective layer. The simulated areas extends over 50 km × 50 km with a 400 m sampling (about ten times more resolved than VenSpec-U's expected best-case spatial resolution) and altitudes ranging from the surface to 100 km (extending below and above the altitude sensitivity range of VenSpec-U centered on 65–75 km). Two typical scenes will be considered, both at noon: one located at the equator where the atmosphere is convectively unstable at the cloud-top due to strong local solar heating (Markiewicz et al., 2007; Titov et al., 2012), and another at a latitude of 75° where it remains stable due to the weaker insolation (Lefèvre et al., 2024). While the first location represents optimal illumination conditions, the second scene will allow the estimation of a worst case in terms of performance, which are only guaranteed for solar zenith angles below 70°. The simulated observations last from 7.1 to 7.5 s considering the spacecraft respectively at periapsis and apoapsis. Over these durations, the atmospheric temporal variability is neglected, and these maps are considered as time-independent.

3.2. Input parameters of the radiative transfer model

The outputs of the mesoscale model shown in Fig. 2 are next converted into input parameters for a radiative transfer model (RTM), based on the pseudo-spherical version of the DISORT code and described in more detail in Conan et al. (2024). This model is used to generate radiance factor spectra depending on the composition and structure of the atmosphere as well as the observation geometry, using input parameters corresponding to the key parameters targeted by the science goals of VenSpec-U, namely:

1. the SO_2 abundance through its mixing ratio at an altitude of 70 km;
2. the UV absorber abundance, parameterized as the imaginary part of the refractive index at 250 nm of the mode 1 particles of the distribution described by Luginin et al. (2016);

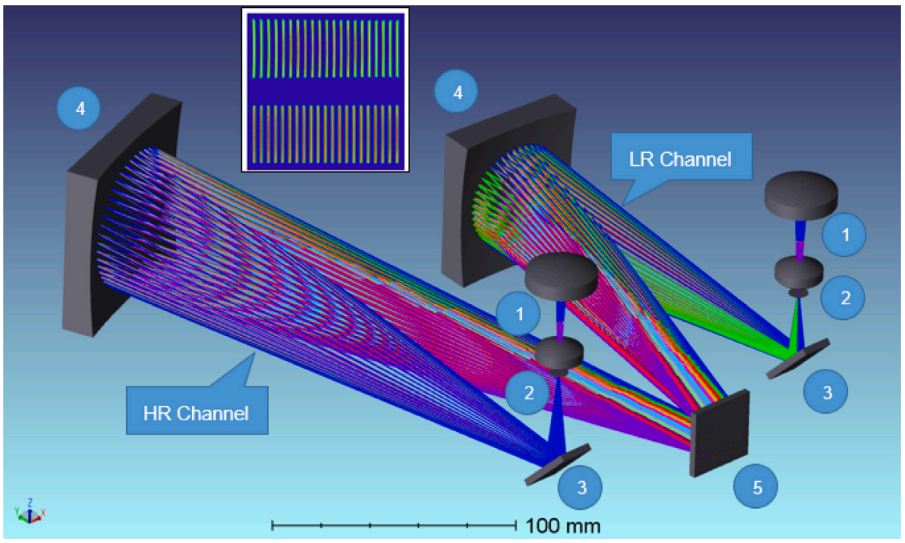


Fig. 1. VenSpec-U's optical design, showing the two-lenses objectives (1), the slits (2), the filters (3), the gratings (4) and the detector (5). *Source:* From Lustrement et al. (2024).

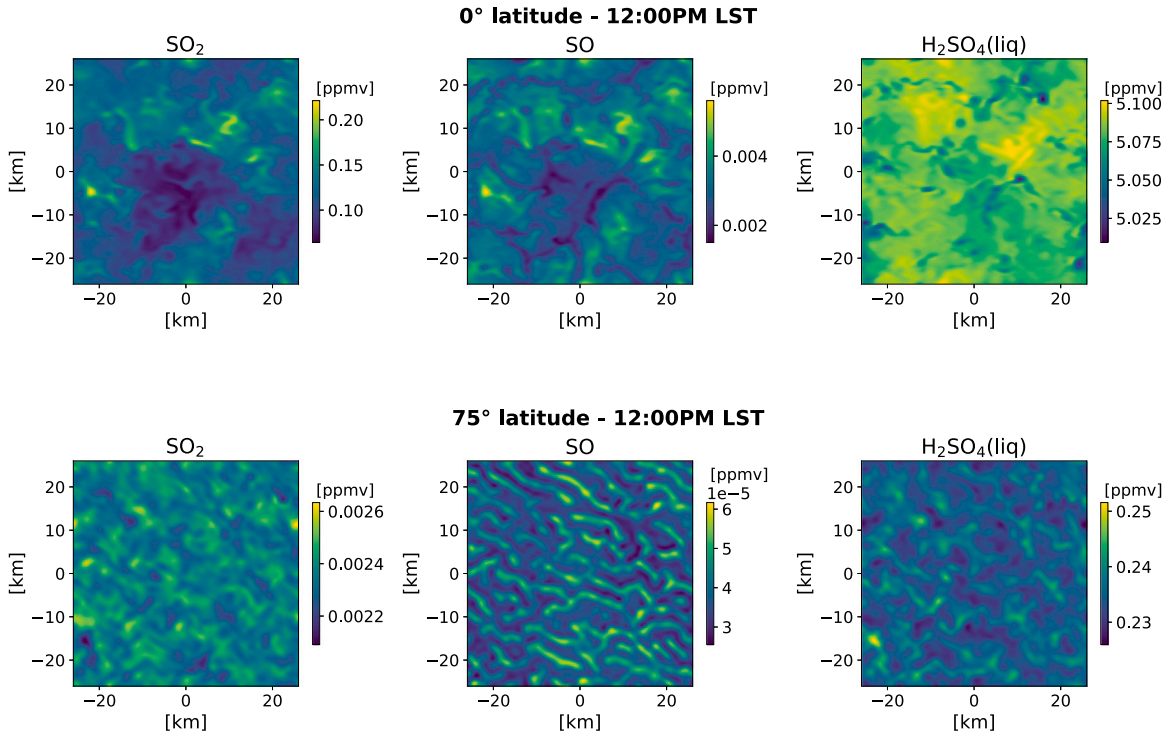


Fig. 2. Sample maps of volume mixing ratios at 70 km altitude simulated by the LES model for the species used to derive the RTM parameters (see Section 3.2): SO_2 (left), SO (center) and the condensed phase of H_2SO_4 (right); at the equator (top row) and 75° latitude (bottom row) at noon.

3. the cloud-top altitude, parameterized as a vertical shift of the vertical profiles for mode 1 and mode 2 particles given by Luginin et al. (2016);
4. the SO/SO_2 columnar abundance ratio.

Some of these parameters, such as the SO_2 abundance and the SO/SO_2 abundance ratio, are direct outputs from the LES model. The cloud-top altitude is computed as described in Lefèvre et al. (2024), using the vertically integrated abundance of the condensed phase of sulfuric acid provided by the LES model, since it is defined as the altitude where optical depth due to the aerosols at a wavelength of 250 nm is equal to one. The UV absorber cannot however be modeled by the LES because of its unknown chemical nature, and the associated RTM parameter must be assumed. It is therefore derived from the map of the spatial distribution of SO_2, as the scales of their spatial variations are considered similar — this is a reasonable assumption since their variations are likely caused by the same dynamical processes, i.e. vertical mixing through convection. The 2D spatial Fourier transform of the SO_2 map is then used, and a random phase is introduced in order to tune the correlation between these two compounds. A fully random phase scramble yields a null correlation, which is a reasonable, agnostic choice regarding the nature of the UV absorber. This parameter tending toward ±1 would indicate either a total correlation or anti-correlation, which could be further investigated depending on the chemical properties of the UV absorber. The simulations described

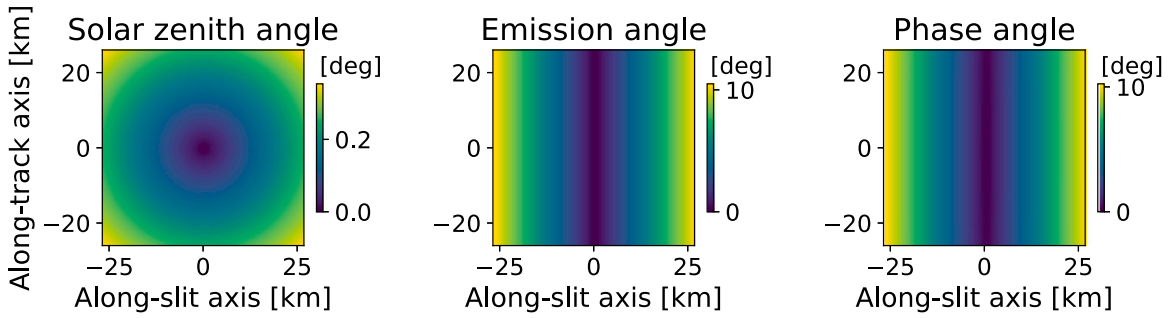


Fig. 3. Maps of input angles for the radiative transfer model, at the equator and local noon, considering the spacecraft at periapsis.

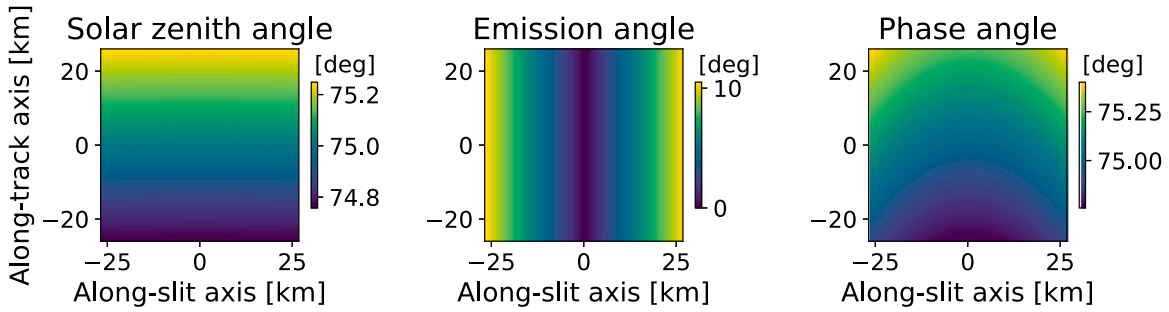


Fig. 4. Maps of input angles for the radiative transfer model, at 75° latitude and local noon, considering the spacecraft at periapsis.

in the following sections were performed with both a null and an exact anti-correlation between the SO_2 and UV absorber. However, it did not seem to impact significantly the results of the simulations, as shown in the examples given in the supplementary materials (Figs. A.30 to A.33). Consequently, only the simulations that consider a null correlation will be shown in the rest of the paper.

The maps are also adjusted to match the spatial extent of the field of view at the cloud-top, depending in particular on the spacecraft altitude. They are therefore either cropped or extended periodically so that no boundary effects appear in the next steps of the simulations. The observation geometry is described with three angles in the 1D pseudo-spherical RTM: the solar zenith angle (SZA), the emission angle, and the phase angle. These parameters are computed for each point of the maps, assuming a nadir pointing configuration over the center of the maps and considering that one of the spatial axis is provided by the orbital scrolling (Figs. 3 and 4).

Multiple scattering in the atmosphere causes the backscattered light to spread, which introduce an intrinsic blur on the observable features and consequently limit the achievable spatial resolution. External studies performed using a 3D Monte Carlo radiative transfer model (He et al., 2026) allowed the determination of the spatial extent of this blur depending on the type of atmospheric component, whether it concerns the gaseous species or the clouds and haze droplets. In order to represent this effect, that VenSpec-U's DISORT-based 1D RTM cannot account for, a Gaussian blur is introduced on the maps of parameters, whose extent depends on the type of atmospheric component, based on the Jacobians shown in the supplementary materials (Fig. A.22): the FWHM is set respectively at 5, 10 and 7.5 km for the UV absorber, gaseous species, and clouds.

Since the output values of the LES model do not necessarily match previous quantitative measurements, the simulated values were adjusted by shifting the medians to correspond to expected values derived from the SPICAV-UV/Venus Express dataset representative of the low and high latitudes. SPICAV-UV was the UV channel of a three-spectrometers set, and operated in the 110–320 nm range with a spectral resolution of 1.5 nm (Bertaux et al., 2007). It performed observations in both nadir viewing and stellar occultation modes and allowed the investigation of the atmospheric composition, including vertical profiles and variability above the cloud-top. At the equator, expected values correspond to 20 ppbv, 72.95 km, and 0.03 respectively for the SO_2 mixing ratio at 70 km, cloud-top altitude and imaginary refractive index representing the UV absorber. At 75° latitude, they correspond to 6.5 ppbv, 64.95 km and 0.009 respectively. As the spectral resolution of SPICAV-UV did not allow the separate measurement of SO and SO_2 abundances, a median of 10% for the SO/SO_2 abundance ratio was considered at both latitudes, in accordance with the interval estimated by Jessup et al. (2015). The resulting maps of parameters are presented respectively in Figs. 5 and 6, at the equator and at 75° latitude. The modification of the contrasts of these atmospheric patterns before the processing by the instrument forward model then allows a precise assessment of the instrument' sensitivity, as presented in Section 6.

Vertical volume mixing ratio profiles $f(z)$ of SO_2 and SO are parameterized as: $f_{SO_2}(z) = f_{SO_2}(70\text{ km}) \cdot \exp\left(\frac{70\text{ km}-z}{3\text{ km}}\right)$ capped at 150 ppm, and $f_{SO}(z) = \frac{f_{SO}(70\text{ km})}{f_{SO_2}(70\text{ km})} \cdot f_{SO_2}(z)$ capped at 1 ppm. The particulate number densities of mode 1 and 2 aerosols droplets are assumed to follow: $n_2(z) = 10^8 \cdot \exp\left(\frac{Z_{top}-4.95\text{ km}-z}{4.5\text{ km}}\right)$ and $n_1(z) = 500 \cdot n_2(z)$ capped at $2 \cdot 10^8$ particles/m^3. The radiative transfer model also includes the contribution of carbonyl sulfide (OCS), following a fixed vertical profile from Haus et al. (2015).

3.3. Data cube generation

Once the maps of the input parameters of the RTM are determined, a radiance factor spectrum is generated in each point with a spectral resolution of 0.1 nm, which is higher than the targeted resolutions of 2 nm for the LR channel and 0.3 nm for the HR channel. It therefore results in a data cube with one spectral dimension and 2 spatial dimensions, one corresponding to the field of view defined by the long-axis of the slit (referred to as "along-slit" or "across-track"), and the other corresponding to the orbital scrolling axis (referred to as "across-slit" or "along-track"). To reduce the computation time, spectra are interpolated from a lookup table generated with the actual RTM, where the solar zenith angle is considered constant over the maps, and the phase angle is either equal to the emission angle for the equator scene,

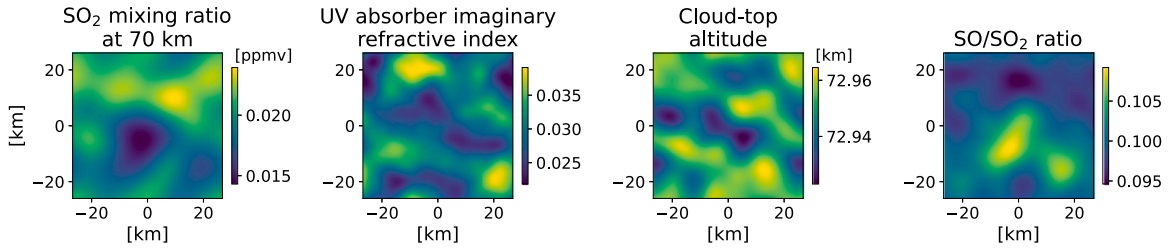


Fig. 5. Maps of input parameters for the radiative transfer model, at the equator and local noon. The typically 10 km across convection cells are clearly visible with updrafts leading to elevated cloud-top altitudes as well as enhanced SO_2 mixing ratio values, and conversely reduced SO/SO_2 ratios.

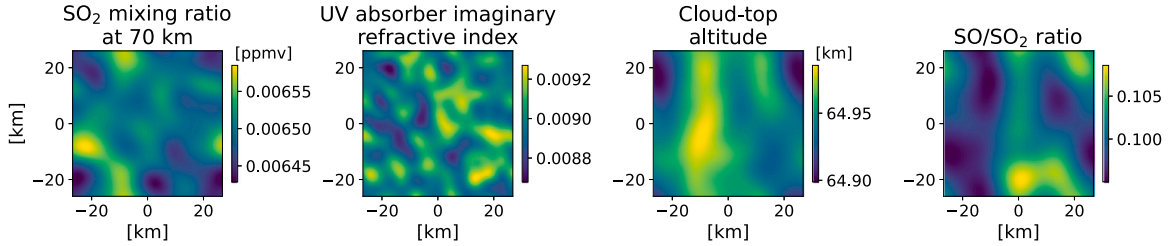


Fig. 6. Maps of input parameters for the radiative transfer model, at 75° latitude and local noon. The spatial variability is caused by gravity waves (spatial wavelength of several tens of km) rather than convection cells as near the equator.

or equal to the SZA for the 75° latitude scene, both being reasonable approximations considering the angles' values shown in Figs. 3 and 4.

These radiance factors are then converted into radiance in order to consider the instrument's actual measurements, as mentioned in Section 2.2. A solar irradiance spectrum derived from SOLAR/SOLSPEC observations and matching this spectral resolution (Meftah et al., 2018) is here used.

4. Instrument forward model

The instrumental effects impacting the produced images are then modeled, by representing successively the influence of the main elements composing the instrument. The model produces independently the LR and HR images from a same scene, using a similar process but different parameters, such as the characteristics of the components or the targeted spectral and spatial samplings from which the acquisition configurations are derived.

4.1. Optical model

The efficiency of the components of the optical chain, namely the lenses, filters, gratings, and the window covering the detector, are first applied to the radiance data cube. The blurring effects in the along-track direction are then taken into account (Fig. 7). They are due to a combination of the motion blur caused by the orbital scrolling during the integration time, as well as the intrinsic blur introduced by the entrance objectives and width of the slit, modeled as Point Spread Functions (PSFs) that vary with the wavelengths and position in the 20° field of view delimited by the long-axis of the slit. The integration time is determined by the desired spatial sampling, and depends on the speed of the spacecraft relative to the clouds. The orbital speed range from 6.96 to 7.28 km/s, leading to relative speeds between 0.85 and 2.71°/s in the instrument's reference frame, considering the spacecraft at apoapsis and periapsis respectively. This total integration time can however be divided into multiple shorter time steps according to the stacking configuration, as detailed in Section 4.3.

These blurred spectral maps are next translated into successive frames, as seen by the detector. After sampling the maps in the along-track direction with a step corresponding to the chosen integration time, radiometric effects are taken into account to determine the amount of photons arriving on each pixel of the detector, including for instance the signal density variations due to the dispersion by the gratings. The quantum efficiency (QE) of the detector is then applied to generate maps of the electrons distribution in the focal plane. The QE is considered at this stage instead of in the following detector model, to allow a precise consideration of its spectral dependency. At this point, the maps are still defined on a regular wavelength grid, but the next step of the model places the spectra on the detector plane, corresponding to the physical pixels. After that, only estimations of the wavelength associated to a pixel can be made. The QE is therefore applied before this fine scale spectral information is lost. After the spectra are positioned on the detector, a second stage of PSFs, modeled beforehand through dedicated raytracing optical analyses and varying with the wavelength and the position in the field of view, is applied to the projections of the images on the focal plane.

Straylight is also considered, including ghost images and internal scattering (Fig. 8). The first ones are due to multiple reflections between the surfaces close to the focal plane, namely the front and back surfaces of the detector' window as well as the detector's surface, and appear as secondary spots with an efficiency loss due to the multiple crossings of the window. Secondly, the amount of scattered light is taken into account through the Total Integrated Scatter (TIS), estimated at 10% with the same extent in the vertical and horizontal directions. No variations with respect to the wavelength or position in the field of view are considered at this stage.

Poisson shot noise is finally added, using the mean number of electrons expected on each pixel of the images as parameters for the distributions.

4.2. Detector

The effects linked to the detector are next simulated, based on the detector's characteristics acquired by the manufacturer Teledyne, at LATMOS or at The Open University. Photo-response non-uniformity (PRNU) and dark signal are first added. The latter is composed of a constant offset (expressed in electrons) and an integration time- and temperature-dependent component (expressed in electrons/second) that doubles every +5.5°C. The various coefficients of the expression of the dark signal are derived for each pixel from dark maps acquired at various integration times.

$$\mathrm{DarkSignal} = \mathrm{DarkOffset} + \mathrm{ThermalDarkSignal}(T_0) \cdot \mathrm{IntegrationTime} \cdot \exp\left(\frac{T - T_0}{7.937\,\mathrm{K}}\right)$$

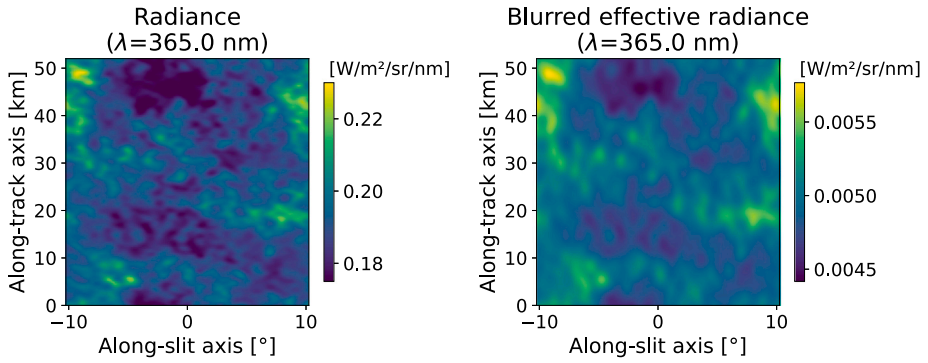


Fig. 7. Effective radiance map before (left) and after (right) applying the along-track blurring effects, for a scene located at the equator and local noon. For illustration purpose, these maps do not take the intrinsic atmospheric blur (Section 3.2) into account.

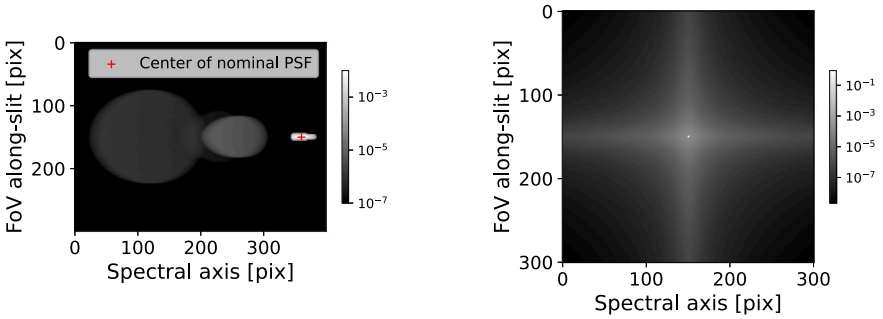


Fig. 8. PSF and associated ghosts for the LR channel at 365 nm and at the center of the field of view (left) ; scattering convolution kernel (right)

where T is the detector's temperature, here set at −25°C, and T_0 is a reference temperature.

The response of the pixels is next applied to translate the theoretical amount of incident electrons into the actual number of electrons collected by each pixel of the detector. It includes non linearity effect as well as pixels' saturation. The modulation transfer function of the detector is then taken into account and random readout noise is added, before the electrons maps are converted into numerical units. Finally, the data are clipped to the maximum value representable by the 14-bit analog to digital converter (ADC).

4.3. Onboard data processing

Lastly, some onboard processing steps are simulated, starting with the binning of pixels into "macropixels", whose size is derived from the targeted spectral and spatial samplings. More advanced process involving intermediate binning steps and corrections are foreseen in the actual instrument in order to minimize various types of errors, due for instance to the quantization or defective pixels, but are however not included in the model yet, as adjustments on the algorithms are still being made. The planned process will include dark frame and row offset subtraction, and 3-by-3 median binning step to remove the influence of defective pixels, before the binning into macropixels of the targeted size derived from the spectral and spatial samplings. Variance stabilization will also be applied before quantization and compression in order to reduce the noise and fixed patterns.

In order to avoid pixel saturation, the total integration time needed to reach the correct spatial sampling can be subdivided so that multiple frames of shorter integration times are stacked together. This effect mostly occurs with the LR channel for wavelengths between 300 and 350 nm where the albedo of Venus is comparatively high and the Sun much brighter than at shorter wavelengths.

5. Inversion model

Maps of the atmospheric RTM parameters must then be retrieved in order to be compared to the initial values provided to the forward RTM for the generation of the data cube (Section 3.3). In the scope of this study, a simple inversion process with minimal corrections of instrumental effects is implemented, to estimate their impact on the quality of the images produced by the instrument, and consequently on the accuracy of the observed atmospheric spatial variations. As it relies on a direct conversion between the numerical units and the radiance for each bin, this inverse model is not an exact inversion of each step of the forward version. Therefore, the retrieved spectra still contains some perturbations, in addition to the binning step that induces a loss of spatial and spectral resolution.

5.1. Simulated radiometric calibration

The simulated images must first be converted from numerical units back to radiance. A conversion factor is estimated by simulating an in-flight calibration, which will rely on Sun observations with two different components to reduce the high intensity of the Sun compared to Venus: a pinhole or a diffuser. As the diffuser configuration is the closest from Venus' observations configuration, covering the whole field of view by spreading the incident light, the same instrumental model is used. The observed scene is then modeled using a high resolution solar irradiance spectra (Meftah et al., 2018) and taking into account the Bidirectional Transmittance Distribution Function (BTDF) of the diffuser as well as its wavelength and angular dependence in order to generate a radiance scene. The BTDF of the diffuser is considered homogeneous over the whole field of view and its transmission was set around 60%, with a ±5% variation between 190 and 380 nm. These characteristics were determined based on typical UV diffusers but should however be updated in the future depending on the selected component.

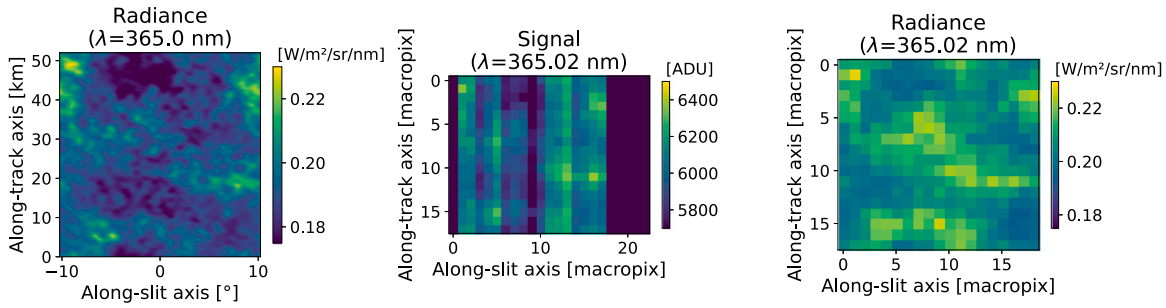


Fig. 9. Example of maps obtained at different stages of a simulation for the LR channel with a 3 km sampling: input radiance (left), measured signal (center), and retrieved radiance (right). The artifacts visible in the measured signal appear to be corrected by the inversion process, resulting in an output radiance map that resembles the input of the simulation.

As the Sun's images resulting from the instrument forward model are associated to a known radiance level, a conversion factor can be estimated. These simulations are run with a similar binning scheme as for the Venus observation, in order for them to be comparable with a minimal algorithm.

Because the dark offset is not negligible and would induce a significant deformation of the retrieved spectra towards the shorter wavelengths, an average dark signal is removed from the simulated images beforehand. Dark frames are then simulated by excluding the optical effects from the instrumental model, using the same integration time, binning and stacking configurations as the Sun or Venus simulations.

The images simulated for the Venus observation case can therefore be converted back to radiance, and as a second step, to radiance factor using a solar spectrum. This latter could be different than the one used for the simulation of the Sun observation case, since the purpose of the solar calibration is not to accurately measure the solar spectral irradiance.

Examples of maps recomposed from the simulated images are presented in Fig. 9. The retrieved radiance is generally higher than the initial because the inversion process approximates the forward model with a linear conversion factor between the output signal and the input radiance, whereas non-linearity occurs mostly toward low signal levels and saturation. As the conversion factor was here determined using high signal levels, the retrieved radiance in areas with lower signal levels tends to be overestimated.

5.2. Fitting strategy

The inverse radiative transfer model is next used to retrieve the atmospheric parameters corresponding to each spectrum. It merely consists in a version of the forward RTM (Section 3.2) coupled to a Levenberg–Marquardt optimization scheme (Newville et al., 2020) minimizing the residual between the synthetic observations and the forward RTM divided by the estimated error level. This latter is the ratio between a typical unbiased radiance factor spectrum corresponding to the considered observation conditions, in this case a SZA of zero, and the expected signal-to-noise ratio in order to represent the noise profile.

The SO_2 mixing ratio and UV absorber imaginary refractive index are left free in the fitting algorithm for both channels, whereas the cloud-top altitude and the SO/SO_2 abundance ratio are estimated with only one channel, respectively LR and HR. The remaining unfitted parameter, the SZA and phase angles are considered constant over the maps, and the emission angle depends on the position in the field of view.

6. Estimation of detection thresholds

After the inversion of each radiance factor spectra by the inverse RTM, the maps of parameters can be reassembled and compared to the initial maps, derived from the LES model (Section 3). A schematic overview of the whole simulation method is presented in Fig. 10.

6.1. Threshold determination and simulation cases

The minimal amplitude of the spatial variations of each targeted atmospheric parameter allowing them to be retrieved through the instrumental effects is then assessed. To do so, the input of the instrumental model is modified by generating various maps of RTM parameters whose contrasts have been either stretched or reduced. The rescaled maps are therefore obtained so that: $\ln(\text{map}_{\text{rescaled}}) = a \cdot \ln(\text{map}_{\text{init}}) + b$ for the SO_2 mixing ratio, imaginary refractive index of mode 1 aerosol droplets, and SO/SO_2 abundance ratio; or $\text{map}_{\text{rescaled}} = a \cdot \text{map}_{\text{init}} + b$ for the cloud-top altitude; where a is a coefficient used to modify the contrasts, and b is a shift applied to maintain the median value at the value derived from SPICAV-UV observations (see Section 3.2). For the SO_2 mixing ratio, imaginary refractive index, and SO/SO_2 abundance ratio, the relative contrasts are expressed relatively as: $\text{contrast} = \frac{3\sigma\left[\ln(\text{map}_{\text{init}})\right]}{\text{median}\left[\ln(\text{map}_{\text{init}})\right]}$. For the cloud-top altitude the contrast is simply defined as: $\text{contrast} = 3\sigma\left[\text{map}_{\text{init}}\right]$. Table 1 displays the range of contrasts explored in the simulations.

Contrasts of the maps are modified for one parameter at a time. The spectra associated to these new maps are then processed with the instrumental model before being inverted with the fitting algorithm, following the method described in the previous sections. The similarity between the initial and retrieved maps is evaluated for each parameter in order to estimate the minimal contrast level detectable by the instrument.

Besides the two scenes shown in Section 3 located at the equator or at a latitude of 75°, two spacecraft altitudes are considered, either at the 220 km periapsis or at the 510 km apoapsis (Figs. A.23 to A.28 showing the parameters and results of the apoapsis simulations are presented in the supplementary materials). With the LR channel, for which the high resolution observation is one of the science objective, the spatial sampling will be considered both at the goal and the requirement, which are respectively 3 and 5 km. For the HR channel, only the goal spatial sampling of 12 km will be considered, as the required 24 km would not allow the estimation of a relevant correlation because too few pixels would be available along the field of view.

6.2. Similarity assessment

In order to estimate the similarity between the two sets of maps, the initial ones are averaged so that they match the sampling of the output of the instrumental model in both the along-track and along-slit directions. The degree of similarity is estimated through the Pearson correlation coefficient, and a correlation level under which the maps cannot be considered similar enough to fulfill VenSpec-U science objectives is defined. To estimate empirically what a given correlation value represents in terms of map similarity, degraded maps resulting

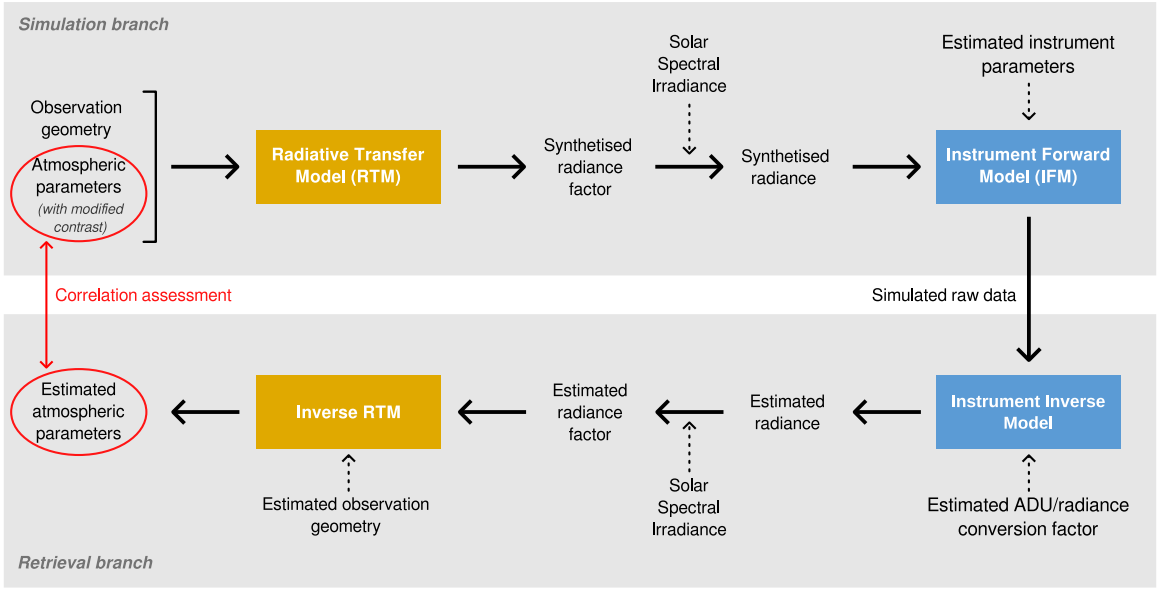


Fig. 10. Overview of the simulation loop. The "Simulation branch" is based on the forward versions of the models (RTM and IFM) and simulates raw images from the assumed atmospheric parameters and observation geometry. The "Retrieval branch" uses the inverse versions of the models to retrieve successively the radiance factors and atmospheric parameters.

Table 1
Contrasts ranges considered for each parameter. The amplitude is here the difference between the maximum and minimum values of the maps. Contrasts variations of the cloud-top altitude and SO/SO_2 abundance ratio are studied only with the LR and HR channel respectively.

		SO_2 mixing ratio	Imaginary refractive index of mode 1 aerosols particles	Cloud-top altitude	SO/SO_2 abundance ratio
Equator, noon					
LR	Median value	20.0 ppbv	0.03	72.95 km	0.1
	Contrast	0.41%–20.29%	0.11%–10.67%	0.08–3.44 km	–
	Amplitude	0.512–22.672 ppbv	0.0002–0.0173	0.124–5.393 km	–
HR	Contrast	0.41%–6.49%	0.11%–8.54%	–	1.92%–24.96%
	Amplitude	0.512–7.787 ppbv	0.0002–0.0138	–	0.0072–0.1074
75° latitude, noon					
LR	Median value	6.5 ppbv	0.009	64.95 km	0.1
	Contrast	0.41%–9.48%	0.04%–6.15%	0.06–2.52 km	–
	Amplitude	0.235–5.822 ppbv	0.0–0.0047	0.087–3.904 km	–
HR	Contrast	0.01%–6.77%	0.77%–15.38%	–	0.21%–27.92%
	Amplitude	0.003–4.06 ppbv	0.0006–0.0119	–	0.0007–0.099

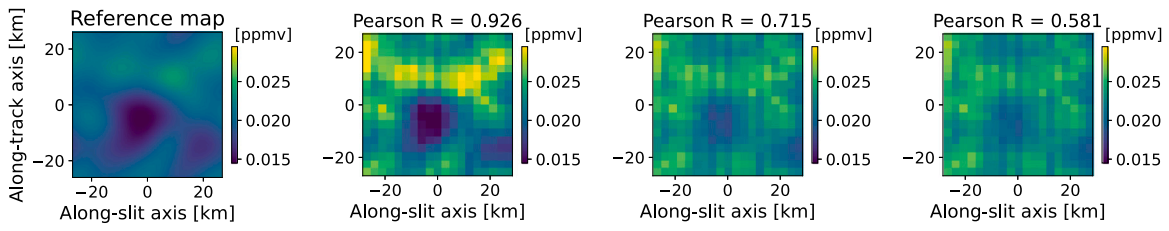


Fig. 11. Comparison between simulated maps with decreasing contrasts and a reference map to determine the targeted correlation levels.

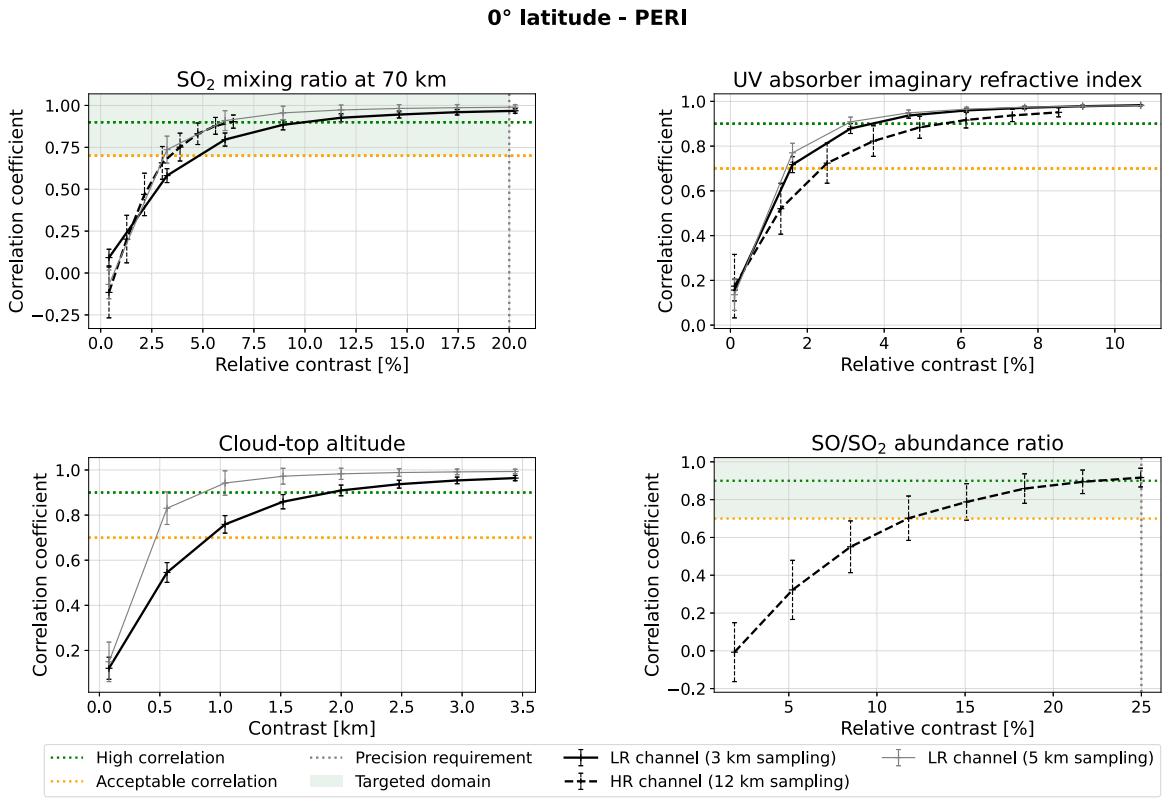


Fig. 12. Evolution of the correlation between the initial and retrieved maps of the four atmospheric parameters targeted by VenSpec-U, for a scene located at the equator observed from the periapsis: SO_2 mixing ratio (top left), UV absorber imaginary refractive index (top right), cloud-top altitude (bottom left), SO/SO_2 abundance ratio (bottom right). The plain and dashed black curves show the correlations respectively for LR and HR channels. The orange and green horizontal dotted lines represent the targeted correlation levels, respectively 0.7 (acceptable) and 0.9 (good). The goals in terms of imaging capabilities are achieved when the acceptable correlation level (0.7) is exceeded with contrasts lower than the required precision (vertical dotted black line).

from several simulations, in which various contrasts were applied at the start, have been compared to the reference input map (Fig. 11). A high level of similarity is considered to be obtained for a correlation coefficient of 0.9, but a correlation above 0.7 is still considered acceptable, as the main spatial features remain discernible. Another set of maps, where random Gaussian noise is added to a binned reference map instead of running the simulation with modified contrasts, is shown in supplementary material (Fig. A.29) to help estimate visually the link between correlation coefficients and map similarity.

6.3. Discussion

The evolution of the correlation between the initial and retrieved maps is shown in Figs. 12 and 13 respectively for the equator at periapsis and 75° latitude at apoapsis, using the goal spatial samplings of 3 km for the LR channel and 12 km for the HR channel. The error bars are the standard deviation of correlations computed between the reference input map and random maps of the considered parameter. The latter are generated by randomly sampling a parameter value for each pixel, from a Gaussian distribution with a mean equal to the fitted value and a standard deviation equal to the uncertainty of the fitting. The resulting thresholds for the other tested configurations are listed in Table 2, where they are compared to the precision requirements defined for the SO_2 and SO/SO_2 retrievals, set respectively at 20% and 25% (EnVision Red Book, ESA, 2023). Satisfactory correlations are achieved for values lower than the requirements for SO_2 and SO/SO_2 with substantial margins in all tested configurations. This is also the case at a latitude of 75°, despite the fact that this location lies outside the instrument's nominal coverage limit of 70° solar zenith angles, resulting in lower illumination and signal-to-noise ratios.

The correlation seems to be slightly better for the periapsis simulations than for the apoapsis. This is expected since the spatial features appear larger when observed from the periapsis, thus covering a larger number of macropixels and improving the correlation statistics. The increase of the spatial sampling, studied with the LR channel simulations, also tends to improve the resulting correlation between the initial and retrieved maps of parameters, as the targeted correlation levels of 0.7 or 0.9 are reached with lower contrasts of the initial maps. The longer integration time indeed allows to reach higher signal-to-noise ratios.

Example of maps simulated with contrasts yielding a 0.9 correlation are shown in Figs. 14 and 15 for a scene at the equator observed from the periapsis using the goal samplings, which are respectively 3 and 12 km for the LR and HR channels. Example of radiance factor spectra are also presented in Fig. 16 for this scene. The retrieved maps are very close to the initial ones, as all parameters are set at their detection thresholds in the same simulation, contrary to the previous tests where only one parameter was modified at a time. The differences observed between the initial values and the retrievals were not addressed in this study, as it was focused on the observability of spatial patterns. With the LR channel, the retrieved values of all parameters are overestimated, which leads to a radiance factor level slightly lower than the expected spectrum (Fig. 16). With the HR channel, the SO/SO_2 abundance ratio is retrieved accurately, but the fitting process seems to compensate the darkening effects of SO_2 and the UV absorber by overestimating the former and underestimating the latter. This should be further investigated in the future.

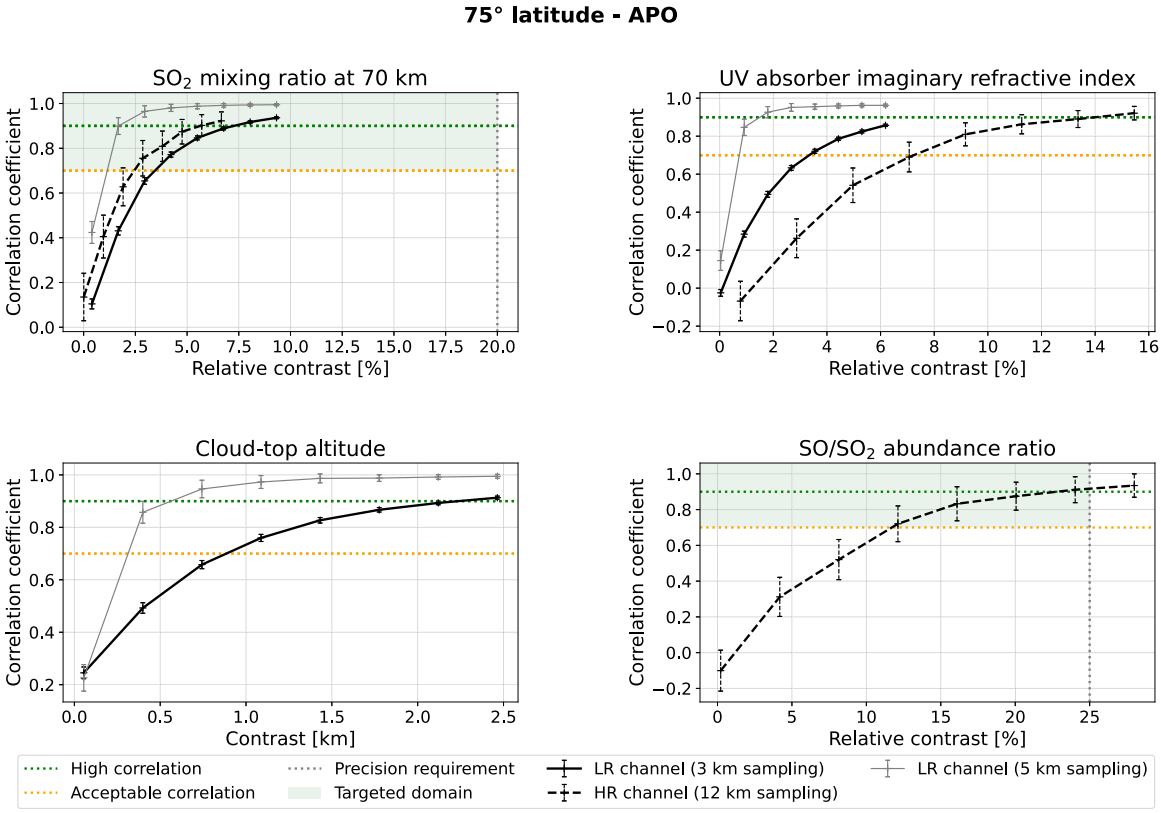


Fig. 13. Evolution of the correlation between the initial and retrieved maps of the four atmospheric parameters targeted by VenSpec-U, for a scene located at 75° latitude observed from the apoapsis: SO_2 mixing ratio (top left), UV absorber imaginary refractive index (top right), cloud-top altitude (bottom left), SO/SO_2 abundance ratio (bottom right).

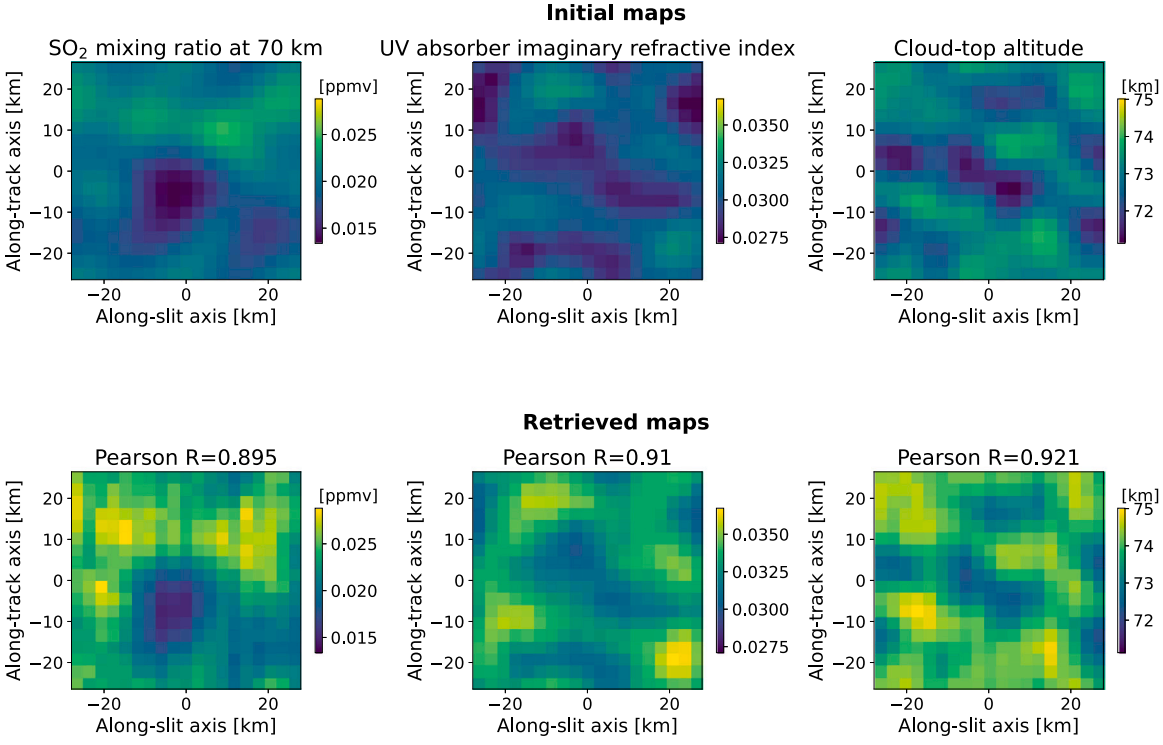


Fig. 14. Comparison between initial (top) and retrieved maps (bottom) of the three atmospheric parameters targeted by the LR channel, for a scene located at the equator observed from the periapsis: SO_2 mixing ratio (left), UV absorber imaginary refractive index (center), cloud-top altitude (right).

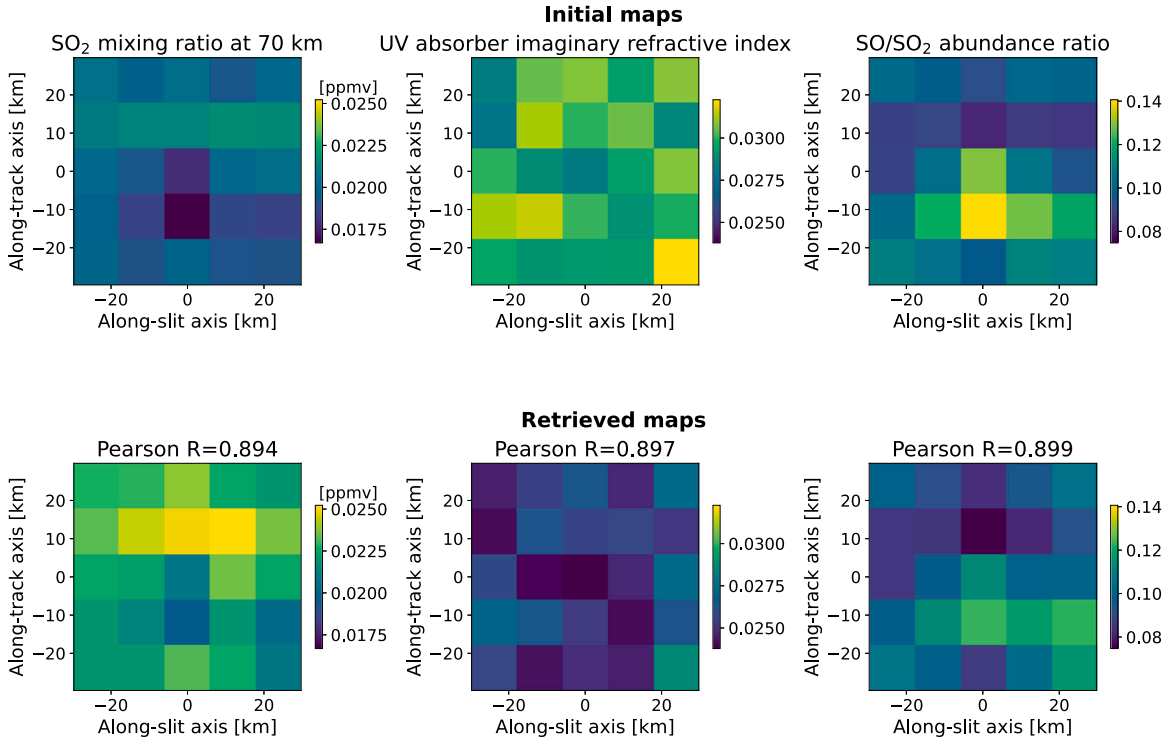


Fig. 15. Comparison between initial (top) and retrieved maps (bottom) of the three atmospheric parameters targeted by the HR channel, for a scene located at the equator observed from the periapsis: SO_2 mixing ratio (left), UV absorber imaginary refractive index (center), SO/SO_2 abundance ratio (right).

Table 2
Contrasts thresholds for the four targeted parameters yielding a 0.7 correlation. Green text indicates that contrasts equivalent to the precision requirement result in a correlation level of 0.9. Black text corresponds to the absence of a defined requirement, in particular for the UV absorber and cloud-top altitude retrievals.

		LR channel		HR channel
RTM parameter	Sampling / Scene	3 km	5 km	12 km
SO_2 mixing ratio [%]	Equator PERI	4.8	3.1	3.4
	Equator APO	10.6	5.2	4.6
	75° latitude PERI	3.0	1.3	1.4
	75° latitude APO	3.4	1.1	2.4
Imaginary refractive index of mode 1 aerosols particles [%]	Equator PERI	1.6	1.4	2.4
	Equator APO	1.9	1.6	5.2
	75° latitude PERI	1.6	0.7	3.4
	75° latitude APO	3.3	0.7	7.2
Cloud-top altitude [km]	Equator PERI	0.9	0.5	Not fitted
	Equator APO	2.1	0.7	
	75° latitude PERI	0.5	0.2	
	75° latitude APO	0.9	0.3	
SO/SO_2 abundance ratio [%]	Equator PERI	Not fitted		11.8
	Equator APO			9.3
	75° latitude PERI			10.4
	75° latitude APO			11.7

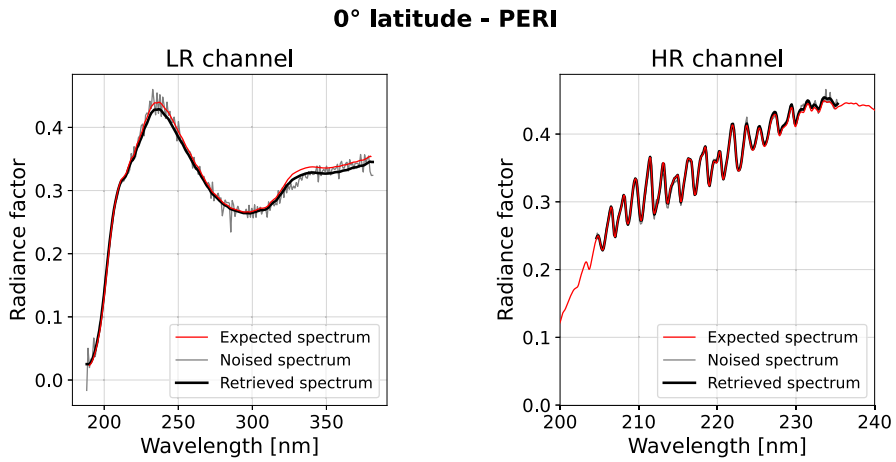


Fig. 16. Initial, noised and fitted radiance factor spectra corresponding to the top left pixels of the maps shown in Figs. 14 and 15, for a simulated scene at the equator observed from the periapsis.

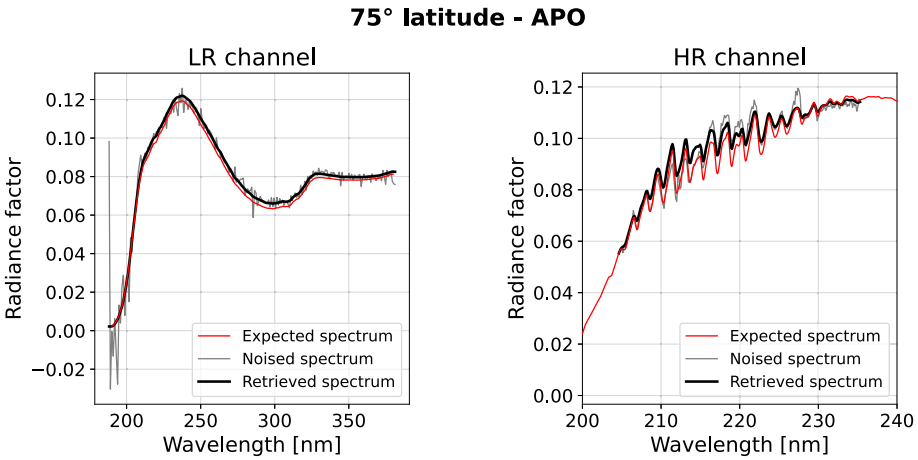


Fig. 17. Initial, noised and fitted radiance factor spectra corresponding to the top left pixels of the maps shown in Figs. A.27 and A.28, for a scene at 75° latitude observed from the apoapsis.

Under degraded observation conditions, namely at 75° latitude (Fig. 17), the signal level is lower due to the high solar zenith angle and the noise is comparatively high at short wavelengths despite the dark removal in the inversion. As the signal-to-noise ratio is taken into account in the fitting algorithm, the retrieved spectra remain close to the expected ones.

6.4. Systematic errors, dispersion and spatial frequency distributions

Additional statistics were analyzed. Differences between the medians and standard deviations of the retrieved maps of RTM parameters and the initial maps averaged at the same sampling, are shown for all simulations in Figs. 18 and 19 for the LR and HR channels respectively. The differences observed in the median values are not related to the contrast of the maps, which suggests that these errors originate from the current inversion process. The over- and-underestimations of the retrieved parameters are consistent with the maps shown in Figs. 14, 15, A.27 and A.28. On the other hand, the standard deviations of the retrieved maps are higher than those of the input maps with low contrasts, but this trend is reversed toward high contrasts, where the retrieved maps exhibit lower standard deviations than the input maps. As small contrasts lead to noisier retrieved maps, higher contrasts conversely result in a reduced dispersion.

Evolution of the spatial frequencies distributions between the initial and retrieved maps have also been studied. These distributions are computed as the radial average of the 2D spatial Fourier transform of each map. Figs. 20 and 21 show the spatial frequencies distributions for the retrieval of the SO_2 mixing ratio in two simulation configurations. For simulations with low contrasts, high frequencies are amplified in the retrieved maps, which reflects the increased noise. With higher contrasts, the distributions of the retrieved maps get closer to the expected ones. Similar behaviors are observed for all parameters and simulation configurations.

7. Conclusion

One of the science goals of the VenSpec-U instrument onboard EnVision will be to perform observations of the Venusian cloud-top at high spatial resolution, in order to observe the small-scale dynamical processes such as gravity waves and convection cells that extend over a few kilometers. The method implemented for the assessment of the instruments' performance for observing these features was presented. To that end, maps of parameters of the radiative transfer model used to generate radiance factor spectra from the atmospheric properties that VenSpec-U aims to measure were derived from cloud-top maps of chemical species modeled by a Large Eddy Simulation, in order to generate a spectral radiance data cube associated to an observed scene.

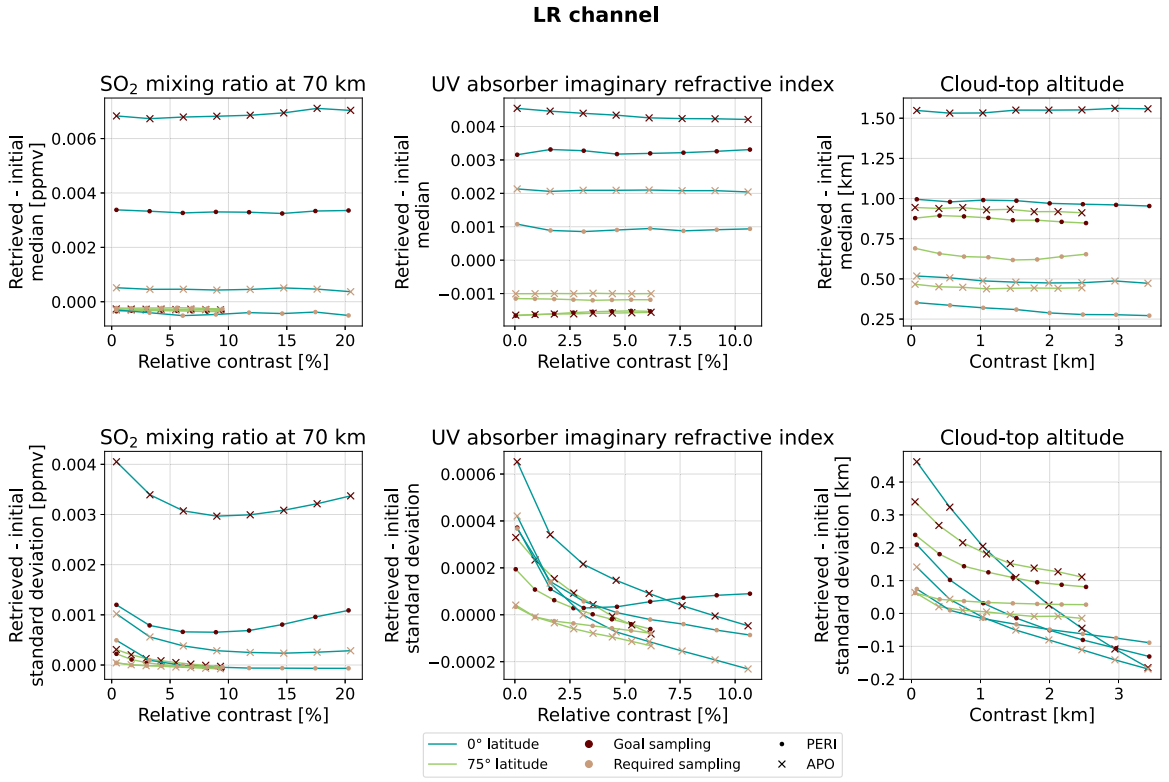


Fig. 18. Evolution of the difference between median values and standard deviations of the retrieved map and the input map averaged at the same spatial sampling, for the simulations of the LR channel. The line color, marker shape and marker color indicate respectively the scene latitude, spacecraft altitude and spatial sampling considered in the simulations.

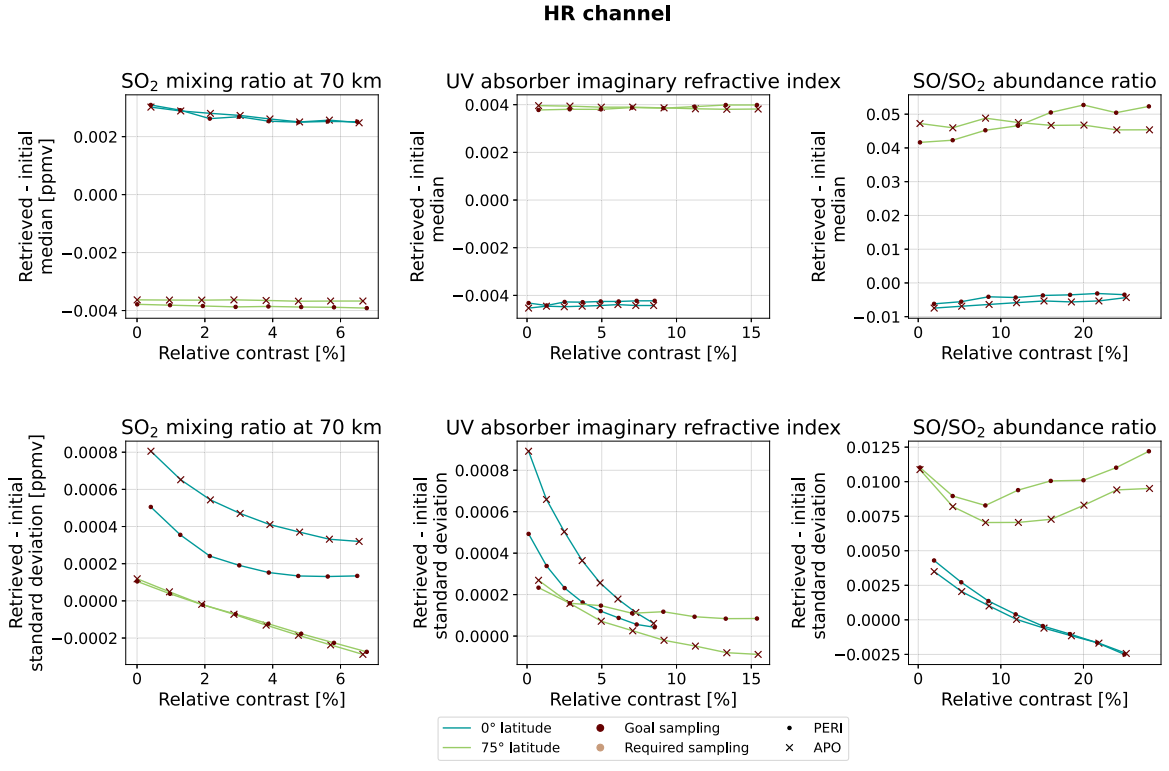


Fig. 19. Evolution of the difference between median values and standard deviations of the retrieved map and the input map averaged at the same spatial sampling, for the simulations of the HR channel. The line color, marker color and marker shape indicate respectively the scene latitude, spatial sampling and spacecraft altitude considered in the simulations.

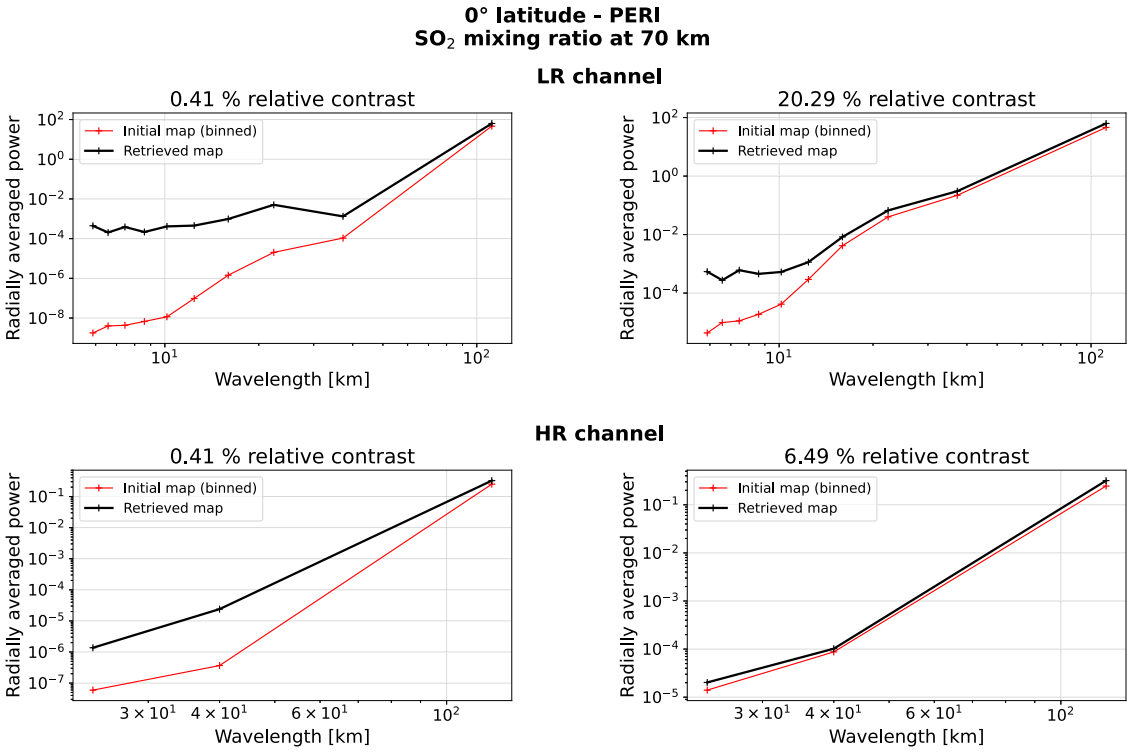


Fig. 20. Power spectra of the Fourier transform of the retrieved and initial maps of SO_2 mixing ratio, for a scene located at the equator and the spacecraft at periapsis, plotted against spatial wavelengths. The left side shows simulations with low contrasts applied to the input maps, while the right side shows simulations with high-contrasts input maps. The minimal wavelengths are consistent with the binning schemes of the simulations, here performed with the goal spatial samplings of 3 and 12 km for the LR and HR channel respectively.

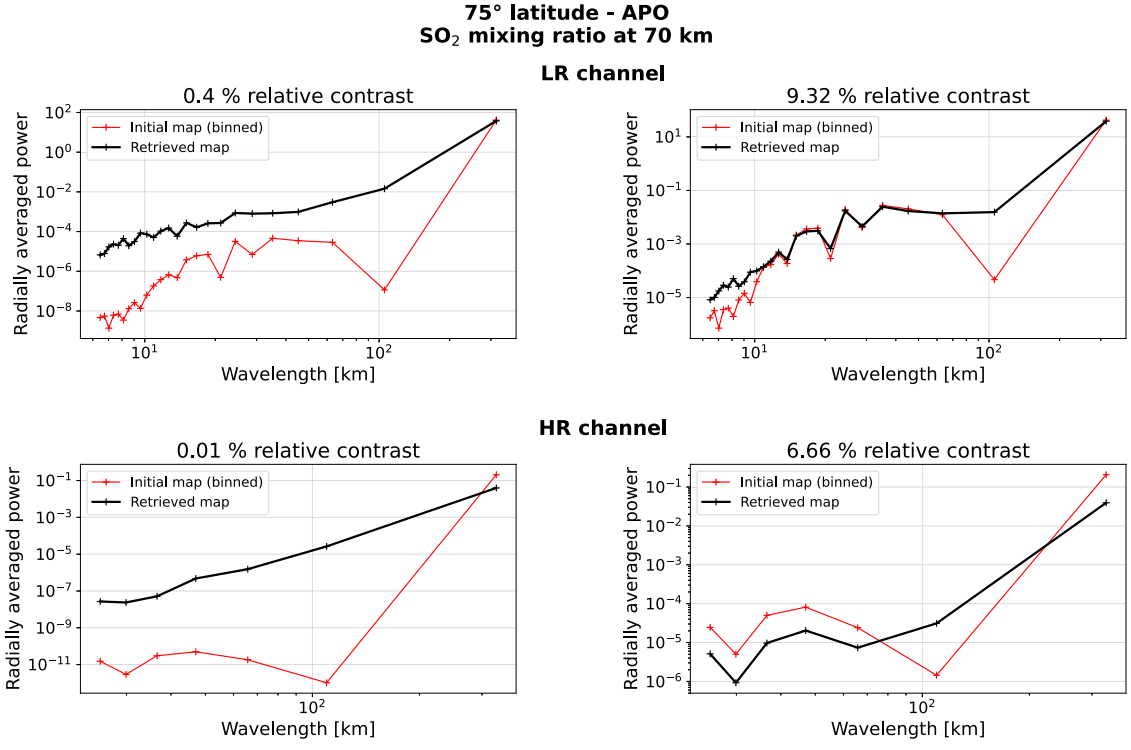


Fig. 21. Power spectra of the Fourier transform of the retrieved and initial maps of SO_2 mixing ratio, for a scene located at 75° latitude and the spacecraft at apoapsis, plotted against spatial wavelengths. The left side shows simulations with low contrasts applied to the input maps, while the right side shows simulations with high-contrasts input maps. The minimal wavelengths are consistent with the binning schemes of the simulations, here performed with the goal spatial samplings of 3 and 12 km for the LR and HR channel respectively.

An instrument forward model has been developed in order to simulate how images of these scenes would be impacted by instrumental effects. A simple inversion process was then used to retrieve the targeted atmospheric parameters. The modification of the contrasts of the maps of RTM parameters, before processing them with the instrument and inversion models, and their comparison with the required precision allowed the estimation of thresholds enabling these atmospheric features to be observed. Simulations were performed with various settings, including different location of the scene, spacecraft altitude and spatial samplings, in particular with the LR channel for which these high resolution observations are more relevant. The instrument is expected to resolve spatial variations in atmospheric properties with the targeted samplings of both LR and HR channels under all tested observation configurations.

This study was performed using the available knowledge about the current state of the instrument. The models should however be refined in the future in order to be more representative, including updated characteristics, additional instrumental effects and more accurate processes. For instance, the 1D radiative transfer model could be updated to be consistent with other existing RTMs in the IR (VenSpec-H/EnVision) and UV (UVI/Akatsuki) domains, and include an extension to the lower cloud, which was found to have a significant impact on the radiance factor for wavelengths above 320 nm. A 3D Monte-Carlo model would also allow a better estimation of multiple scattering effects as well as cast shadows due to the variations in cloud-top altitude at high solar zenith angles. The instrument forward model could be completed with additional detector effects, such as the quantum yield, row offsets and lag. More representative data processing algorithms, including onboard dark subtraction and the intermediate median binning step, and the planned inversion pipeline should also be used for future studies. The performance is consequently expected to improve with these algorithms, which will include various corrections of instrumental effects. A simulation loop including VenSpec-U's radiative transfer model, instrument forward model and their respective inverse versions, will then allow the improvement of the study of the performance and sensitivity of the instrument, as well as those of the data processing algorithms and quality of the biases corrections.

CRediT authorship contribution statement

Lucile Conan: Writing – original draft, Visualization, Validation, Software, Methodology, Investigation, Formal analysis, Data curation. **Emmanuel Marcq:** Writing – review & editing, Supervision, Methodology, Funding acquisition, Conceptualization. **Benjamin Lustrement:** Writing – review & editing, Supervision. **Maxence Lefèvre:** Software, Methodology, Conceptualization. **Nicolas Rouanet:** Validation, Supervision, Methodology. **Baptiste Leduc:** Methodology. **Abraham Diaz Damian:** Methodology. **Lucio Baggio:** Validation, Methodology, Conceptualization. **Sandrine Bertran:** Project administration. **Séverine Robert:** Project administration. **Océane Barraud:** Project administration. **Giulia Alemanno:** Project administration.

Declaration of competing interest

The authors declare that they have no known competing financial interests or personal relationships that could have appeared to influence the work reported in this paper.

Acknowledgments

LC acknowledges support by a doctoral grant from Centre National d'Études Spatiales (CNES) and from DIM (Domaine d'Intérêt Majeur) ORIGINES labeled by the Île-de-France region (funding grant IDF-DIM-ORIGINES-2022-1-03). EM, BL, NR, SB acknowledge CNES and ESA (European Space Agency) funding for all activities related to VenSpec-U and EnVision. ML acknowledges receiving funding from the European Union's Horizon Europe research and innovation program under the Marie Skłodowska-Curie grant agreement 101110489/MuSICA-V.

Appendix. Supplementary materials

A.1. 3D radiative transfer model Jacobians

See Fig. A.22.

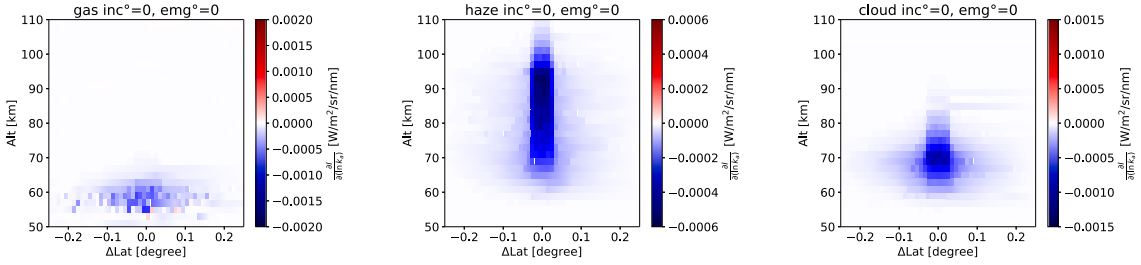


Fig. A.22. Spatial spread of the rays due to multiple scattering estimated by the 3D radiative transfer model, depending on the type of atmospheric compound: gas (left), haze (center), clouds (right). (Credits: Z. He).

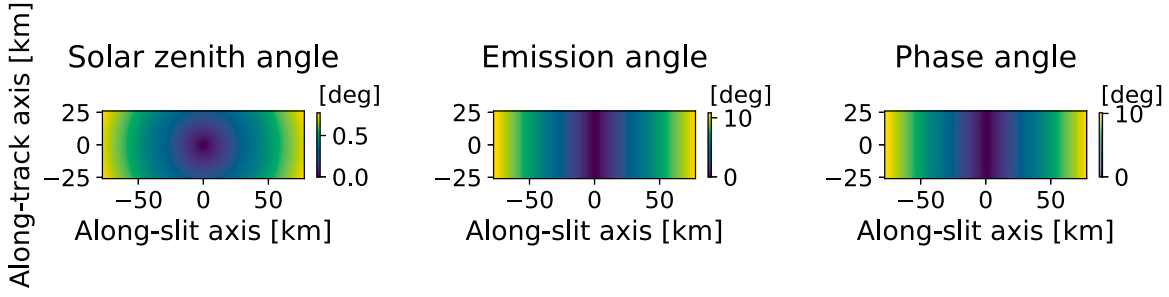


Fig. A.23. Maps of input angles for the radiative transfer model, at the equator and local noon, considering the spacecraft at apoapsis.

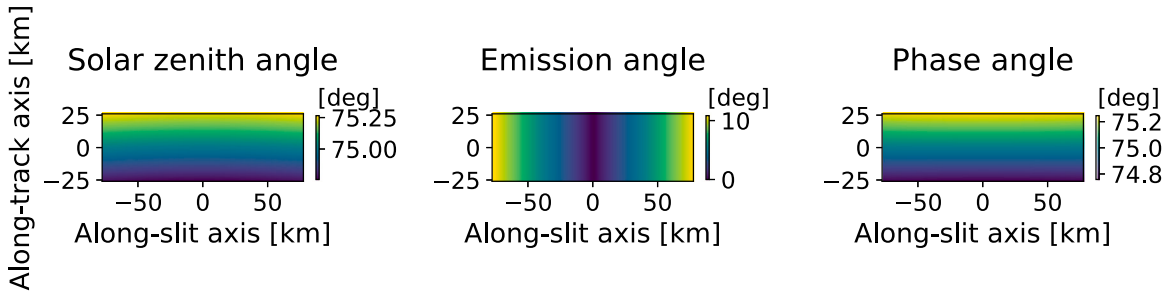


Fig. A.24. Maps of input angles for the radiative transfer model, at 75° latitude and local noon, considering the spacecraft at apoapsis.

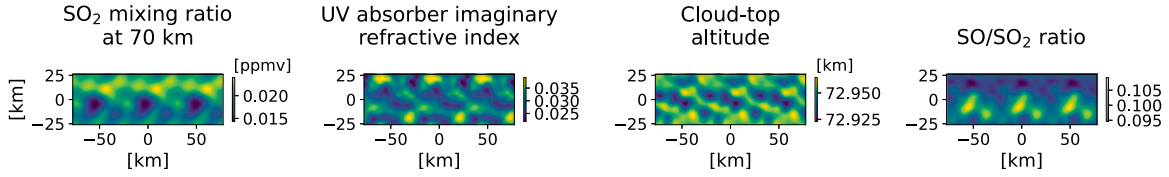


Fig. A.25. Maps of input parameters for the radiative transfer model, at the equator and local noon, considering the spacecraft at apoapsis. The maps are similar as the ones used for the periapsis simulations, but are extended periodically in the across-track direction to fill the 20° instantaneous field of view of VenSpec-U.

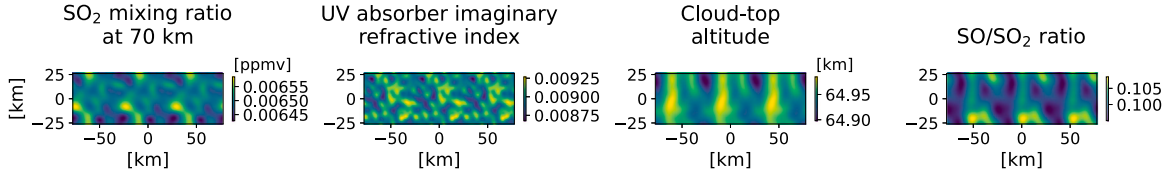


Fig. A.26. Maps of input parameters for the radiative transfer model, at 75° latitude and local noon, considering the spacecraft at apoapsis. The maps are similar as the ones used for the periapsis simulations, but are extended periodically in the across-track direction to fill the 20° instantaneous field of view of VenSpec-U.

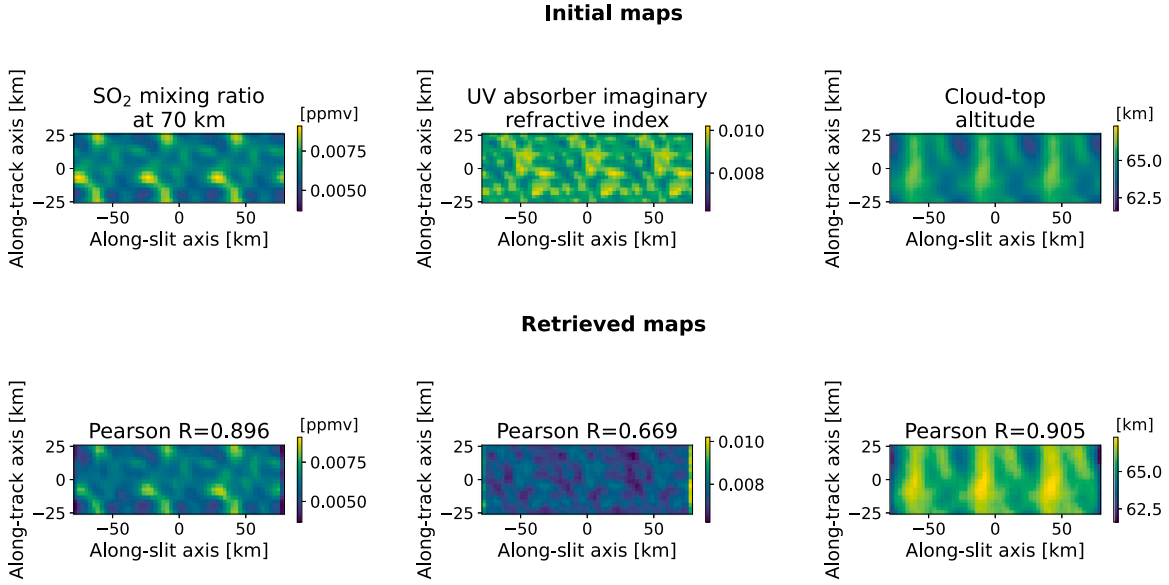


Fig. A.27. Comparison between initial (top) and retrieved maps (bottom) of the three atmospheric parameters targeted by the LR channel, for a scene located at 75° latitude observed from the apoapsis: SO_2 mixing ratio (left), UV absorber imaginary refractive index (center), cloud-top altitude (right).

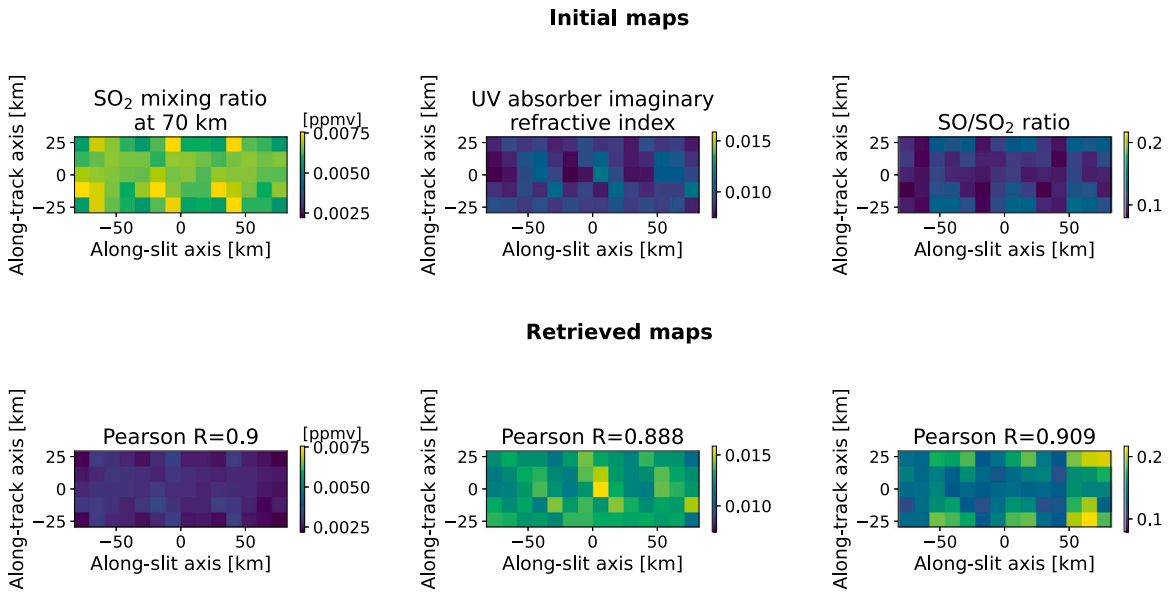


Fig. A.28. Comparison between initial (top) and retrieved maps (bottom) of the three atmospheric parameters targeted by the HR channel, for a scene located at 75° latitude observed from the apoapsis: SO_2 mixing ratio (left), UV absorber imaginary refractive index (center), SO/SO_2 abundance ratio (right).

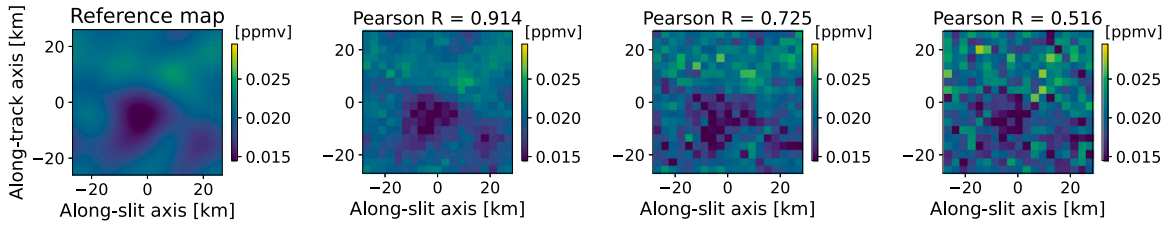


Fig. A.29. Comparison between a reference map and the same map on which random Gaussian noise of increasing variances is added, to determine the targeted correlation levels.

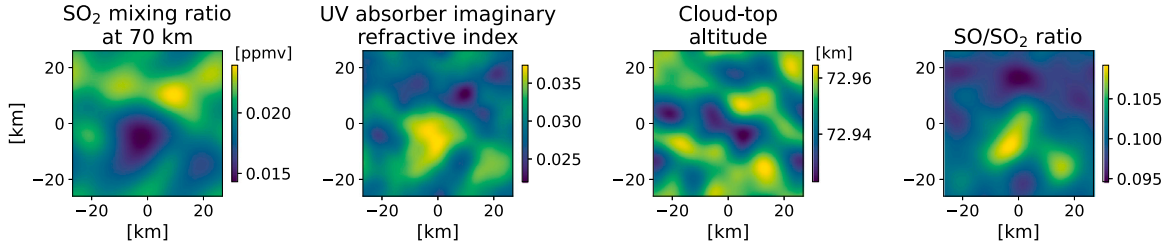


Fig. A.30. Maps of input parameters for the radiative transfer model, at the equator and local noon, with an exact anti-correlation between SO_2 and the UV absorber.

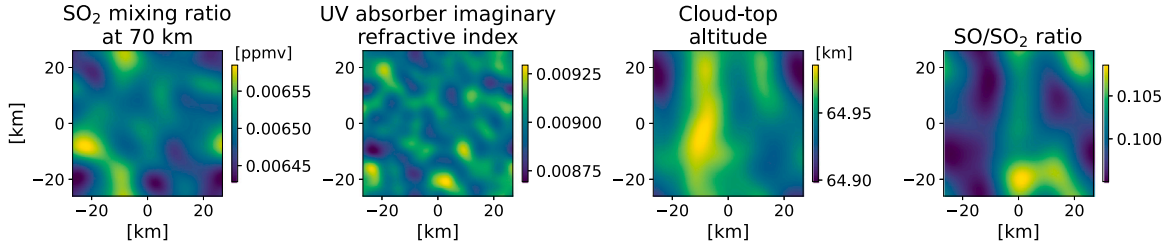


Fig. A.31. Maps of input parameters for the radiative transfer model, at 75° latitude and local noon, with an exact anti-correlation between SO_2 and the UV absorber.

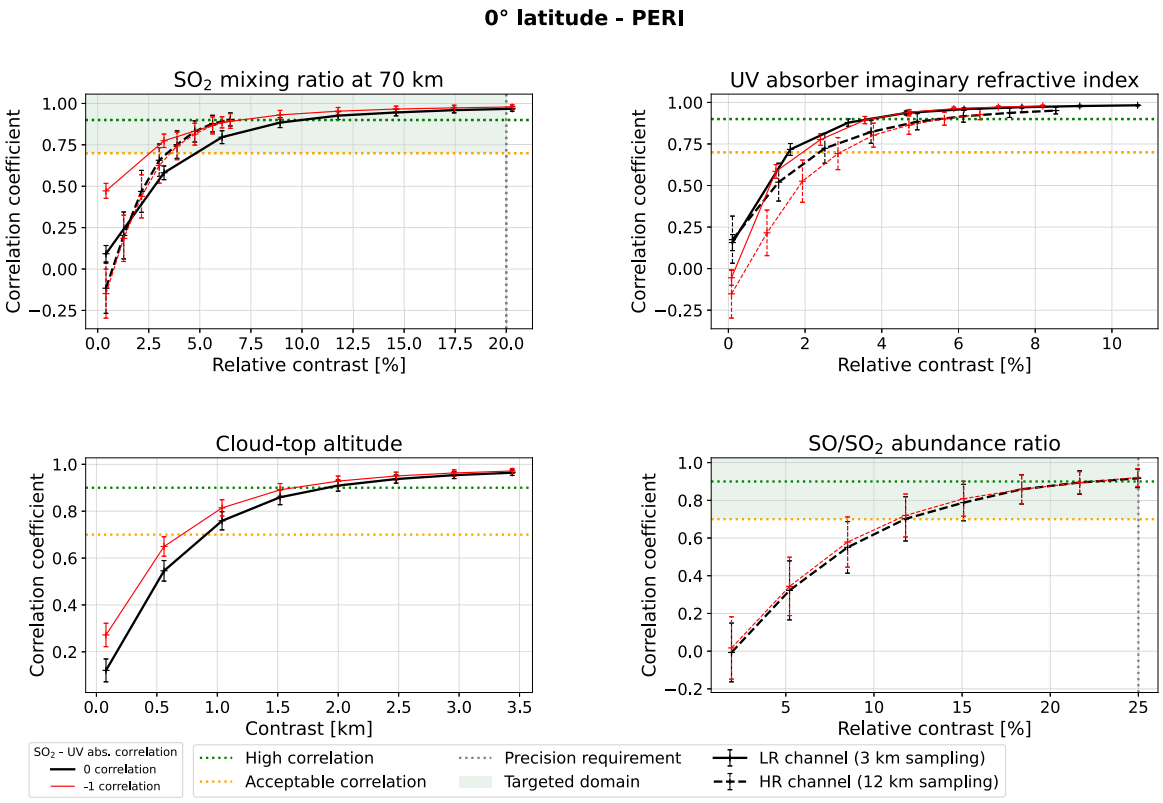


Fig. A.32. Evolution of the correlation between the initial and retrieved maps of the four atmospheric parameters targeted by VenSpec-U, for a scene located at the equator observed from the periapsis: SO_2 mixing ratio (top left), UV absorber imaginary refractive index (top right), cloud-top altitude (bottom left), SO/SO_2 abundance ratio (bottom right).

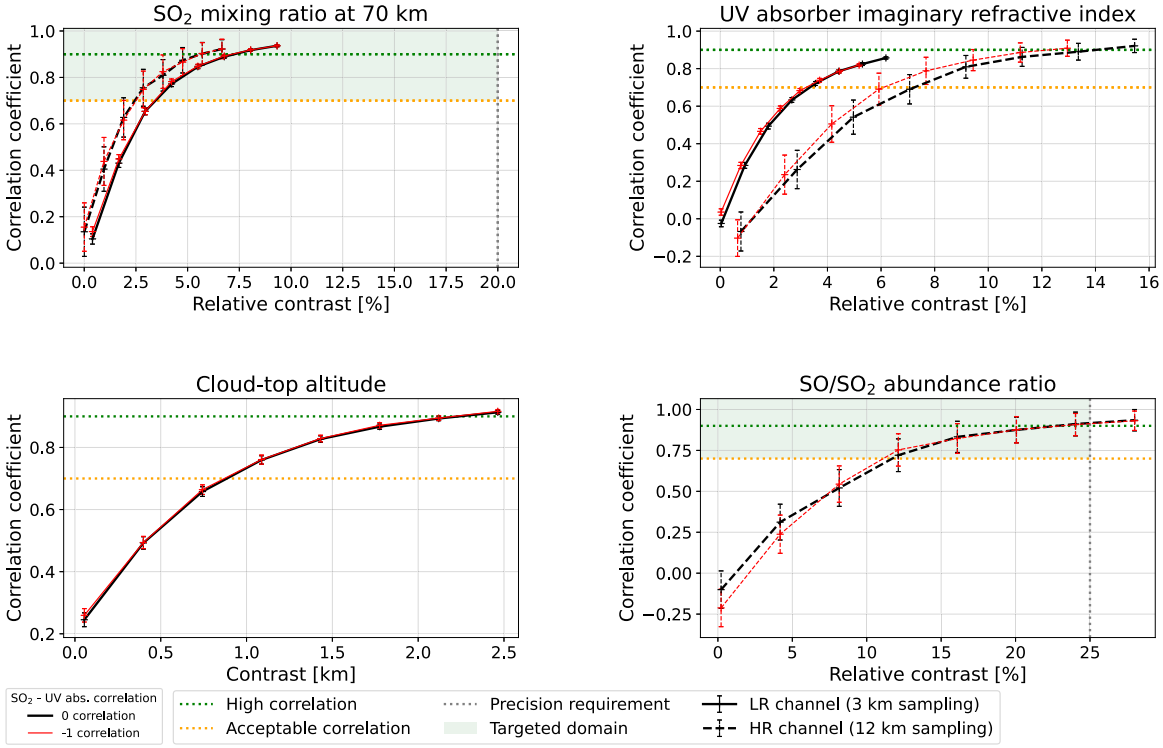


Fig. A.33. Evolution of the correlation between the initial and retrieved maps of the four atmospheric parameters targeted by VenSpec-U, for a scene located at 75° latitude observed from the apoapsis: SO_2 mixing ratio (top left), UV absorber imaginary refractive index (top right), cloud-top altitude (bottom left), SO/SO_2 abundance ratio (bottom right).

A.2. Parameters and results of apoapsis simulations

See Figs. A.23–A.28.

A.3. Definition of satisfactory Pearson correlation coefficients

See Fig. A.29.

A.4. Effect of the spatial correlation between SO_2 and the UV absorber

See Figs. A.30–A.33.

Data availability

The authors do not have permission to share data.

References

Bertaux, J.-L., Nevejans, D., Korablev, O., Villard, E., Quémerais, E., Neefs, E., Montmessin, F., Leblanc, F., Dubois, J.P., Dimarellis, E., Hauchecorne, A., Lefèvre, F., Rannou, P., Chaufray, J.Y., Cabane, M., Cernogora, G., Souchon, G., Semelin, F., Reberac, A., Van Ransbeek, E., Berkenbosch, S., Clairquin, R., Muller, C., Forget, F., Hourdin, F., Talagrand, O., Rodin, A., Fedorova, A., Stepanov, A., Vinogradov, I., Kiselev, A., Kalinnikov, Y., Durry, G., Sandel, B., Stern, A., Gérard, J.C., 2007. SPICAV on venus express: Three spectrometers to study the global structure and composition of the Venus atmosphere. Planet. Space Sci. 55 (12), 1673–1700. http://dx.doi.org/10.1016/j.pss.2007.01.016, URL: https://www.sciencedirect.com/science/article/pii/S0032063307000074.

Conan, L., Marcq, E., Lustrement, B., Rouanet, N., Parc, L., Bertran, S., Robert, S., Helbert, J., Alemanno, G., 2024. The VenSpec-U spectrometer onboard envision: Sensitivity studies. In: Infrared Remote Sensing and Instrumentation XXXII. Vol. 13144, SPIE, pp. 197–239. http://dx.doi.org/10.1117/12.3027500, URL: https://www.spiedigitallibrary.org/conference-proceedings-of-spie/13144/131440L/The-VenSpec-U-spectrometer-onboard-EnVision-sensitivity-studies/10.1117/12.3027500.full.

EnVision Red Book, ESA, 2023. EnVision: Understanding Why Earth's Closest Neighbour is So Different. Technical Report, ESA, URL: https://www.cosmos.esa.int/documents/10892653/0/EnVision+Red+Book_ESA-SCI-DIR-RP-003+(1).pdf/b037b151-f4fe-303a-f6c6-430c605a407f?t=1706621315626.

Haus, R., Kappel, D., Arnold, G., 2015. Radiative heating and cooling in the middle and lower atmosphere of Venus and responses to atmospheric and spectroscopic parameter variations. Planet. Space Sci. 117, 262–294. http://dx.doi.org/10.1016/j.pss.2015.06.024.

He, Z., Vinatier, S., Eymet, V., Forest, V., Bézard, B., Rannou, P., Rodriguez, S., Marcq, E., Fournier, R., Blanco, S., Mourtaday, N., Nyffenegger-Péré, Y., Lebonnois, S., Määttänen, A., 2026. Simultaneous estimation of radiance and its sensitivities to radiative properties in a spherical-heterogeneous atmospheric radiative transfer model by monte carlo method: application to titan. J. Quant. Spectrosc. Radiat. Transf. 350, 109722. http://dx.doi.org/10.1016/j.jqsrt.2025.109722, https://www.sciencedirect.com/science/article/pii/S002240732500384X.

Helbert, J., Vandaele, A.C., Marcq, E., Robert, S., Ryan, C., Guignan, G., Rosas-Ortiz, Y.M., Neefs, E., Thomas, I.R., Arnold, G., Peter, G., Widemann, T., Lara, L.M., 2019. The VenSpec suite on the ESA EnVision mission to Venus. In: Strojnik, M., Arnold, G.E. (Eds.), Infrared Remote Sensing and Instrumentation XXVII. SPIE, San Diego, United States, p. 6. http://dx.doi.org/10.1117/12.2529248, URL: https://www.spiedigitallibrary.org/conference-proceedings-of-spie/11128/2529248/The-VenSpec-suite-on-the-ESA-EnVision-mission-to-Venus/10.1117/12.2529248.full.

Jessup, K.L., Marcq, E., Mills, F., Mahieux, A., Limaye, S., Wilson, C., Allen, M., Bertaux, J.-L., Markiewicz, W., Roman, T., Vandaele, A.-C., Wilquet, V., Yung, Y., 2015. Coordinated hubble space telescope and venus express observations of venus' upper cloud deck. Icarus 258, 309. http://dx.doi.org/10.1016/j.icarus.2015.05.027.

Lefèvre, M., Lefèvre, F., Marcq, E., Määttänen, A., Stolzenbach, A., Streel, N., 2024. Impact of the turbulent vertical mixing on chemical and cloud species in the venus cloud layer. Geophys. Res. Lett. 51 (12), http://dx.doi.org/10.1029/2024gl108771, URL: https://agupubs.onlinelibrary.wiley.com/doi/10.1029/2024GL108771. Publisher: American Geophysical Union (AGU).

Lefèvre, M., Spiga, A., Lebonnois, S., 2017. Three-dimensional turbulence-resolving modeling of the Venusian cloud layer and induced gravity waves. J. Geophys. Res.: Planets 122 (1), 134–149. http://dx.doi.org/10.1002/2016JE005146, URL: https://onlinelibrary.wiley.com/doi/abs/10.1002/2016JE005146. _eprint: https://onlinelibrary.wiley.com/doi/pdf/10.1002/2016JE005146.

Luginin, M., Fedorova, A., Belyaev, D., Montmessin, F., Wilquet, V., Korablev, O., Bertaux, J.L., Vandaele, A.C., 2016. Aerosol properties in the upper haze of Venus from SPICAV IR data. Icarus 277, 154–170. http://dx.doi.org/10.1016/j.icarus.2016.05.008, URL: https://www.sciencedirect.com/science/article/pii/S0019103516301488.

Lustrement, B., Bertran, S., Rouanet, N., Damián, A.D., Hassen-Khodja, R., Montaron, C., Ruocco, S., Vontrat, A., Vivat, F., Baggio, L., Guignan, G., Simonnet, E., Conan, L., Gabier, C., Langlois, A., Mathon, R., Nguyen-Tuong, N., Recart, W., Buey, T., Vinatier, S., Lasue, J., Lara, L., Marcq, E., Robert, S., Helbert, J., 2024. Design of the VenSpec-u instrument: A double UV imaging spectrometer to analyze sulfured gases in the Venus' atmosphere. In: Infrared Remote Sensing and Instrumentation XXXII. Vol. 13144, SPIE, pp. 164–196. http://dx.doi.org/10.1117/12.3028252, URL: https://www.spiedigitallibrary.org/conference-proceedings-of-spie/13144/131440K/Design-of-the-VenSpec-U-instrument–a-double-UV/10.1117/12.3028252.full.

Marcq, E., Montmessin, F., Lasue, J., Bézard, B., Jessup, K.L., Lee, Y.J., Wilson, C.F., Lustrement, B., Rouanet, N., Guignan, G., 2021. Instrumental requirements for the study of Venus' cloud top using the UV imaging spectrometer VeSUV. Adv. Space Res. 68 (1), 275–291. http://dx.doi.org/10.1016/j.asr.2021.03.012, URL: https://www.sciencedirect.com/science/article/pii/S0273117721002192.

Markiewicz, W.J., Titov, D.V., Ignatiev, N., Keller, H.U., Crisp, D., Limaye, S.S., Jaumann, R., Moissl, R., Thomas, N., Esposito, L., Watanabe, S., Fiethe, B., Behnke, T., Szemerey, I., Michalik, H., Perplies, H., Wedemeier, M., Sebastian, I., Boogaerts, W., Hviid, S.F., Dierker, C., Osterloh, B., Böker, W., Koch, M., Michaelis, H., Belyaev, D., Dannenberg, A., Tschimmel, M., Russo, P., Roatsch, T., Matz, K.D., 2007. Venus monitoring camera for venus express. Planet. Space Sci. 55 (12), 1701–1711. http://dx.doi.org/10.1016/j.pss.2007.01.004, URL: https://www.sciencedirect.com/science/article/pii/S0032063307000086.

Meftah, M., Damé, L., Bolsée, D., Hauchecorne, A., Pereira, N., Sluse, D., Cessateur, G., Irbah, A., Bureau, J., Weber, M., Bramstedt, K., Hilbig, T., Thiéblemont, R., Marchand, M., Lefèvre, F., Sarkissian, A., Bekki, S., 2018. SOLAR-ISS: A new reference spectrum based on SOLAR/SOLSPEC observations. Astron. Astrophys. 611, A1. http://dx.doi.org/10.1051/0004-6361/201731316, URL: https://www.aanda.org/articles/aa/abs/2018/03/aa31316-17/aa31316-17.html. Publisher: EDP Sciences.

Newville, M., Otten, R., Nelson, A., Ingargiola, A., Stensitzki, T., Allan, D., Fox, A., Carter, F., Michał, Pustakhod, D., Ram, Y., Glenn, Deil, C., Stuermer, Beelen, A., Frost, O., Zobrist, N., Mark, Pasquevich, G., Hansen, A.L.R., Spillane, T., Caldwell, S., Polloreno, A., andrewhannum, Fraine, J., deep 42-thought, Maier, B.F., Gamari, B., Persaud, A., Almarza, A., 2020. Lmfit/lmfit-py 1.0.1. http://dx.doi.org/10.5281/zenodo.3814709, URL: https://zenodo.org/records/3814709.

Peralta, J., Hueso, R., Sánchez-Lavega, A., Piccioni, G., Lanciano, O., Drossart, P., 2008. Characterization of mesoscale gravity waves in the upper and lower clouds of Venus from VEX-VIRTIS images. J. Geophys. Res.: Planets 113 (E5), 2008JE003185. http://dx.doi.org/10.1029/2008JE003185, URL: https://agupubs.onlinelibrary.wiley.com/doi/10.1029/2008JE003185.

Piccialli, A., Titov, D.V., Sanchez-Lavega, A., Peralta, J., Shalygina, O., Markiewicz, W.J., Svedhem, H., 2014. High latitude gravity waves at the venus cloud tops as observed by the venus monitoring camera on board venus express. Icarus 227, 94–111. http://dx.doi.org/10.1016/j.icarus.2013.09.012, URL: https://www.sciencedirect.com/science/article/pii/S0019103513003928.

Tellmann, S., Häusler, B., Hinson, D.P., Tyler, G.L., Andert, T.P., Bird, M.K., Imamura, T., Pätzold, M., Remus, S., 2012. Small-scale temperature fluctuations seen by the VeRa radio science experiment on venus express. Icarus 221 (2), 471–480. http://dx.doi.org/10.1016/j.icarus.2012.08.023, URL: https://linkinghub.elsevier.com/retrieve/pii/S0019103512003429.

Titov, D.V., Markiewicz, W.J., Ignatiev, N.I., Song, L., Limaye, S.S., Sanchez-Lavega, A., Hesemann, J., Almeida, M., Roatsch, T., Matz, K.-D., Scholten, F., Crisp, D., Esposito, L.W., Hviid, S.F., Jaumann, R., Keller, H.U., Moissl, R., 2012. Morphology of the cloud tops as observed by the Venus express monitoring camera. Icarus 217 (2), 682–701. http://dx.doi.org/10.1016/j.icarus.2011.06.020, URL: https://linkinghub.elsevier.com/retrieve/pii/S0019103511002375.

Widemann, T., Smrekar, S., Garvin, J., Straume, A., Ocampo, A., Schulte, M., Voirin, T., Hensley, S., Dyar, M., Whitten, J., Nunes, D., Getty, S., Arney, G., Johnson, N., Kohler, E., Spohn, T., O'Rourke, J., Wilson, C., Way, M., Desai, N., 2023. Venus evolution through time: Key science questions, selected mission concepts and future investigations. Space Sci. Rev. 219, http://dx.doi.org/10.1007/s11214-023-00992-w.

Yamazaki, A., Yamada, M., Lee, Y.J., Watanabe, S., Horinouchi, T., Murakami, S.-y., Kouyama, T., Ogohara, K., Imamura, T., Sato, T.M., Yamamoto, Y., Fukuhara, T., Ando, H., Sugiyama, K.-i., Takagi, S., Kashimura, H., Ohtsuki, S., Hirata, N., Hashimoto, G.L., Suzuki, M., Hirose, C., Ueno, M., Satoh, T., Abe, T., Ishii, N., Nakamura, M., 2018. Ultraviolet imager on Venus orbiter Akatsuki and its initial results. Earth Planets Space 70 (1), 23. http://dx.doi.org/10.1186/s40623-017-0772-6.